

# Data-driven prediction of unsteady flow fields over a circular cylinder using deep learning

Sangseung Lee\* and Donghyun You\*

*\*Department of Mechanical Engineering, Pohang University of Science and Technology,  
77 Cheongam-ro, Nam-gu, Pohang, Gyeongbuk 37673, Republic of Korea*

---

## Abstract

Unsteady flow fields over a circular cylinder are trained and predicted using four deep learning networks: networks associated with supervised feature extraction with and without prior knowledge of physical conservation laws, networks associated with unsupervised feature extraction with and without prior knowledge of conservation laws. Flow fields at Reynolds numbers 100, 200, 300, and 400 are trained, while flow fields at Reynolds numbers 500 and 3000 are predicted. Physical loss functions are proposed to explicitly impose prior knowledge of physical conservation laws to deep learning networks, while an adversarial training is applied to extract features of physical conservation laws in an unsupervised manner without any prior knowledge of the conservation laws. Effects of the proposed loss functions and adversarial training are analyzed. Flow field predictions using deep learning networks show good agreement with flow fields calculated by numerical simulations. Especially, unsupervised feature extractions can be applied to extract undiscovered prior knowledge in data, where many practical data lacks informa-

tion of full underlying physics. The present study suggests that deep learning techniques can be utilized for predicting wake flow.

*Keywords:* Deep learning; supervised feature extraction; unsupervised feature extraction; unsteady flow fields; prior knowledge.

---

## 1. Introduction

Observations of fluid flow in nature, laboratory experiments, and numerical simulations have provided evidence of existence of flow features and certain, but often complex, ordinance. For example, in nature, Kelvin-Helmholtz waves in the cloud [1], von Karman vortices in ocean flow around an island [2], and swirling great red spot on the Jupiter [3] are flow structures that can be classified as a certain type of vortical motions. Similar observations also have been reported in laboratory experiments and numerical simulations [4, 5, 6, 7]. The existence of distinct and dominant flow features that are linearly independent have also been widely investigated by mathematical decomposition techniques such as the proper orthogonal decomposition (POD) method [8], dynamic mode decomposition (DMD) [9], or Koopman operator method [10].

Such distinct or dominant flow features have been utilized by some species such as insects, birds, and fish to control their bodies adequately to better adapt the fluid dynamic environment and to improve the aero- or hydrodynamic performance and efficiency [11, 12]. This suggests that species in nature estimate future flow based on information of experienced flow in the

past by empirically learning dominant flow features in their living environments. However, the learning procedures of species in nature are not based on numerical simulations or mathematical decomposition techniques. Such observation of unsteady flow estimation in nature motivates us to investigate the feasibility of predicting unsteady fluid motions based on flow field information in the past, by extracting flow features using deep learning techniques. Prediction of unsteady flow fields using deep learning could offer new opportunities for real-time control and guidance of aero- or hydro-vehicles, weather forecast, *etc.*

The aim of this study is to propose and compare deep learning techniques for predicting unsteady flow fields. Unsteady flow fields over a circular cylinder are trained and predicted using four deep learning networks: networks associated with supervised feature extraction with and without prior knowledge of physical conservation laws, networks associated with unsupervised feature extraction with and without prior knowledge of conservation laws. Physical loss functions are proposed to impose prior knowledge of physical conservation laws to deep learning networks. Adversarial training of two deep learning models, generator and discriminator models, is applied to extract features of physical conservation laws in an unsupervised manner. Effects of physical loss functions and adversarial training on flow field prediction are qualitatively and quantitatively analyzed. The paper is organized as follows. Deep learning backgrounds are reviewed in section 2. Numerical methods for Navier-Stokes simulations are explained in section 3. The method for

construction of training datasets is explained in section 4. The present deep learning method and its results are presented in sections 5 and 6, respectively, followed by concluding remarks in section 7.

## 2. Deep learning backgrounds

In 1986, Rumelhart et al. [13] developed a machine learning technique, which is widely known as multilayer perceptrons (MLP). MLP is an early stage neural network that firstly applied error backpropagation for training neural networks with sigmoid activation functions. Error of a neural network is evaluated from a loss function that compares values predicted from a neural network and true values from ground truth data. Weights inside a network are updated in the direction of the gradient that minimizes the loss function respect to each weight.

The development of backpropagation for training neural networks have led to a huge growth in the application of neural networks in a variety scientific disciplines. Initial studies of the use of neural networks with sigmoid activation functions to fluid mechanics had been conducted since the late 1990s to the early 2000s [14, 15, 16, 17, 18]. However, neural networks with sigmoid activation functions are known to suffer from a pitfall that gradients of a loss function inevitably vanishes after many error backpropagations through layers. As a consequence, the vanishing gradient problem limited applications of neural networks to complex problems that require networks with many layers for extracting complex feature of data.

In 2012, the vanishing gradient problem has been mostly resolved by the development of a rectified linear unit (ReLU) activation function [19]. The development of ReLU activation function was a breakthrough that provided efficient training and enabled deep learning of neural networks. Consequently, the last five years seen a huge growth in neural networks and there has been a rapid rise in the use of neural networks in fluid mechanics. Tracey et al. [20] and Zhang and Duraisamy [21] utilized shallow neural networks for turbulence modeling for a Reynolds-average Navier-Stokes (RANS) simulation. Ling et al. [22] employed a deep neural network (DNN) with ten hidden layers to model the Reynolds stress anisotropy tensor. These approaches were found to notably improve the accuracy of simulation results.

The principal characteristics of deep learning are extracting feature in a low dimensional feature space. The high dimensional information of an input data is encoded in low dimensional features inside weights of neural networks. Especially, convolutional neural networks (CNNs) are widely considered to be the best architecture to extract features from spatial data like images. There have been some discussions on utilizing CNNs for directly predicting flow characteristics; Guo et al. [23] employed a CNN to predict steady flow fields around bluff objects and reported reasonable predictions with significantly reduced computational cost than that required for numerical simulations; Miyanawala and Jaiman [24] employed a CNN to predict aerodynamic force coefficients of bluff bodies, also with notably reduced computational costs.

Prediction of unsteady flow fields using deep learning involves extracting

both of spatial and temporal features of input flow fields, which could be considered as learning videos. Therefore, a deep learning based video modeling architectures could be a practical method to predict unsteady flow fields. Video modeling enables prediction of a future frame of a video based on information of previous video frames by learning spatial and temporal features of videos. However, even deep learning have been reported to generate high quality real-world like images in image modeling area [25, 26, 27, 28], deep learning architectures for video modeling have shown difficulties in generating high quality predictions as they show blurry predictions [29, 30, 31] due to complex temporal features of data.

A long-short-term memory (LSTM) recurrent neural network based video modeling architecture was proposed by Srivastava et al. [29]. However, the method have shown very blurry reconstruction and predictions of the future video frames. Similarly, Ranzato et al. [30] proposed an architecture that both leverages a recurrent neural network and CNN for learning both of the temporal and spatial features of a video. But they reported that predictions of the future frame tends to slow down the motion and converges to a still blurry image. Mathieu et al. [31] proposed a video modeling architecture that utilizes a generative adversarial network (GAN) with multi-scale CNNs to generate predictions of future frames. GAN is a network that contains a generator and discriminator model, which is proposed by Goodfellow et al. [32]. The generator network generates images and the discriminator network is employed to discriminate the generated images from real (ground truth)

images. GAN is adversarially trained so the generator network is trained to delude the discriminator network, and the discriminator network is trained not to be deluded by the generator network. Nash equilibrium inherently presence in the two pronged adversarial training and it leads the network to extract underlying low-dimensional features in an unsupervised manner, in consequence, better quality images can be generated. Mathieu et al. [31] reported the performance of predicting future frames of videos has improved compared to Ranzato et al. [30] by utilizing GANs with multi-scale CNNs and a gradient difference loss (GDL) function. The GDL function slightly resolves blurriness due to a single usage of mean squared error (MSE) loss function on training video data, as the MSE loss function is highly possible to simply blur an image to minimize the loss function. However, video modeling networks have tended to focus on predicting videos of human motions rather than physical phenomena that follows conservation laws.

### 3. Numerical simulations

Numerical simulations of flow over a circular cylinder at  $Re_D = U_\infty D / \nu = 100, 200, 300, 400, 500$ , and 3000, where  $U_\infty$ ,  $D$ , and  $\nu$  are the freestream velocity, cylinder diameter, and kinematic viscosity, respectively, have been conducted by solving the incompressible Navier-Stokes equations as follows:

$$\frac{\partial u_i}{\partial t} + \frac{\partial u_i u_j}{\partial x_j} = -\frac{1}{\rho} \frac{\partial p}{\partial x_i} + \nu \frac{\partial^2 u_i}{\partial x_j \partial x_j} \quad (1)$$

and

$$\frac{\partial u_i}{\partial x_i} = 0, \quad (2)$$

where  $u_i$ ,  $p$ , and  $\rho$  are the velocity, pressure, and density, respectively. A fully implicit fractional step method is employed as a time integration technique, whereas all terms in the Navier-Stokes equations are integrated using the Crank-Nicolson method. Second-order central-difference schemes are employed for spatial discretization [33]. The computational domain consists of a block structured H-grid with an O-grid around the cylinder (figure 1). The computational domain sizes are  $50D$ ,  $60D$ , and  $6D$  in the streamwise, cross-flow, and spanwise directions, respectively. The computational time-step size ( $\Delta t U_\infty / D$ ) of 0.005 is used for simulations. The domain size, number of grid points, and time-step sizes are determined from an extensive sensitivity study.

#### 4. Datasets

Simulation results of flow over a cylinder at each Reynolds number are collected during 101 time-steps, with time-step intervals of  $\delta t = \Delta t U_\infty / D = 0.01$ . Flow variables ( $u_1(= u)$ ,  $u_2(= v)$ ,  $u_3(= w)$  and  $p$ ) at each time-step and Reynolds number in a square domain of  $-1.5D < x < 5.5D$ ,  $-3.5D < y < 3.5D$ ,  $z = 0D$  ( $7D \times 7D$  sized domain) are extracted into a uniform grid with a size of  $250 \times 250$  grid cells. Thus, a dataset of each Reynolds number

consists of 101 flow fields with size of  $250 \times 250 \times 4$ (= height  $\times$  width  $\times$  flow variables).

Datasets of flow fields at  $Re = 100, 200, 300$ , and  $400$  compose a training dataset. Flow fields in the training dataset are randomly subsampled in time and space to five consecutive flow fields on a  $32 \times 32$  sized grid and  $0.896D \times 0.896D$  sized domain (see figure 2). The subsampled flow fields contain diverse types of flow such as, free stream flow, wake flow, boundary layer flow, or separating flow. Therefore, deep learning networks utilized in the present study are possible to efficiently learn physics from diverse types of flow. The first four consecutive sets of flow fields are input ( $\mathcal{I}$ ) containing the information of flow fields in both space and time, and the last set of flow fields is a ground truth flow field ( $\mathcal{G}(\mathcal{I})$ ). A pair of input and ground truth flow fields form a training sample. In the present study, total 500,000 training samples are employed for training various deep learning networks. Performances of networks are evaluated on a test dataset, which is composed of flow fields at  $Re = 500$  and  $3000$ , without any subsampling in space ( $250 \times 250$  sized grid and  $7D \times 7D$  sized domain).

## 5. Deep learning methodology

### 5.1. Deep learning networks for flow prediction

The employed deep learning networks for flow prediction are variations of the architecture for video modeling proposed by Mathieu et al. [31]. The network structures in the present study consist of a generator model that ac-

cepts four consecutive sets of flow fields as input. Each input set of flow fields is composed of flow variables of  $\{u, v, w, p\}$ , to take advantage of learning correlated physical phenomena between each flow variable. The utilized generator model in this study is composed of set of multi-scale generative CNNs  $\{G_0, G_1, G_2, G_3\}$  to learn multi-range spatial dependencies of flow structures. During training, a generative CNN,  $G_k$ , generates prediction of flow fields ( $G_k(\mathcal{I})$ ) on a  $\frac{32}{2^k} \times \frac{32}{2^k}$  sized grid.  $G_k$  is fed with four consecutive sets of flow fields on a  $\frac{32}{2^k} \times \frac{32}{2^k}$  sized grid ( $\mathcal{I}_k$ ), which are bilinearly interpolated from the original  $32 \times 32$  sized input sets of flow fields ( $\mathcal{I}$ ), and a set of upscaled flow fields,  $R_{k+1} \circ G_{k+1}(\mathcal{I})$  (see figure 3). Note that the domain sizes of the  $\frac{32}{2^k} \times \frac{32}{2^k}$  and  $32 \times 32$  grids are identical and the corresponding convolution kernel size ranges are from 3 to 7 (table 2). Consequently,  $G_k$  is possible to learn larger spatial dependencies of flow fields than  $G_{k-1}$  by sacrificing resolutions. As a result, the multi-scale CNN based generator models learn and predict flow fields with multi-range spatial dependencies. Various configurations of generator models with different set of numbers of feature map sizes ( $N_{16}$ ,  $N_{32}$ , and  $N_{64}$ , see table 1) and numbers of weight layers ( $GM_{16}$ ,  $GM_{18}$ , and  $GM_{20}$ , see table 2) have been trained in the current study.

Let  $\mathcal{G}_k(\mathcal{I})$  be the ground truth flow fields resized on a grid size of  $\frac{32}{2^k} \times \frac{32}{2^k}$ . The discriminator model consists of set of discriminative networks  $\{D_0, D_1, D_2, D_3\}$  with CNNs and fully connected (FC) layers. A discriminative network,  $D_k$ , is fed with inputs of the predicted flow fields from the generative CNN ( $G_k(\mathcal{I})$ ) and the ground truth flow fields ( $\mathcal{G}_k(\mathcal{I})$ ). The CNNs of a discriminative

network extracts low-dimensional features of the predicted flow fields and ground truth flow fields. Then, the connected FC layers compare the extracted low-dimensional features to classify the ground truth flow fields into class 1 and the predicted flow fields into class 0. The output of each discriminative network is a single continuous scalar between 0 and 1, where an output value larger than a threshold (0.5) is classified into class 1 and an output value smaller than the threshold is classified into class 0. Procedures of the discriminator model to classify flow field predictions are summarized in figure 4. Various configuration of the discriminator model with different set of numbers of feature map and layer sizes have been trained (table 3). The generator models are trained with an Adam optimizer [34] with the learning rate, which is a hyperparameter that determines the network update speed, of  $4 \times 10^{-5}$  and the discriminator model is trained with the gradient descent method with the learning rate of 0.02.

### 5.2. Loss functions

For a given set of input and ground truth flow fields, the generator model generates prediction of flow fields that minimize a loss function that is a combination of six different loss functions as follows:

$$\mathcal{L}_{generator} = \frac{1}{N} \sum_{k=0}^{N-1} \{ \lambda_{l2} \mathcal{L}_2 + \lambda_{gdl} \mathcal{L}_{gdl} + \lambda_c \mathcal{L}_c + \lambda_{mom} \mathcal{L}_{mom} + \lambda_{ke} \mathcal{L}_{ke} + \lambda_{adv} \mathcal{L}_{adv}^G \}, \quad (3)$$

where  $N(= 4)$  is the number of scales and

$$\lambda_{l2} + \lambda_{gdl} + \lambda_c + \lambda_{mom} + \lambda_{ke} + \lambda_{adv} = 1. \quad (4)$$

Various loss functions are tested by tuning parameters of  $\lambda_{l2}$ ,  $\lambda_{gdl}$ ,  $\lambda_c$ ,  $\lambda_{mom}$ ,  $\lambda_{ke}$ , and  $\lambda_{adv}$ . Especially,  $\lambda_{adv} = 0.0$  indicates no adversarial training.

$\mathcal{L}_2$  minimizes the difference between predicted flow fields and ground truth flow fields as

$$\mathcal{L}_2 = \|G_k(\mathcal{I}) - \mathcal{G}_k(\mathcal{I})\|_2^2. \quad (5)$$

$\mathcal{L}_{gdl}$  is the GDL function [31]. The loss function is applied to sharpen flow fields by directly penalizing the gradient differences between predicted flow fields and ground truth flow fields as

$$\begin{aligned} \mathcal{L}_{gdl} = \sum_{i=0}^{n_x-1} \sum_{j=0}^{n_y-1} & \left| |\mathcal{G}_k(\mathcal{I})_{(i+1,j+1)} - \mathcal{G}_k(\mathcal{I})_{(i,j+1)}| - \right. \\ & \left. |G_k(\mathcal{I})_{(i+1,j+1)} - G_k(\mathcal{I})_{(i,j+1)}| \right| + \\ & \left| |\mathcal{G}_k(\mathcal{I})_{(i+1,j+1)} - \mathcal{G}_k(\mathcal{I})_{(i+1,j)}| - \right. \\ & \left. |G_k(\mathcal{I})_{(i+1,j+1)} - G_k(\mathcal{I})_{(i+1,j)}| \right|, \end{aligned} \quad (6)$$

where the subscript  $(i, j)$  indicates the grid index of a flow field, and  $n_x$  and  $n_y$  indicate the number of grid points in  $x$  and  $y$  directions. Loss functions  $\mathcal{L}_2$  and  $L_\infty$  provide prior knowledge to networks that predicted flow fields should resemble ground truth flow fields. These loss functions support the networks

to learn physics, which corresponds to the prior knowledge, by extracting features in a supervised manner.

Let  $u_k, v_k, w_k, p_k$  be non-dimensionalized flow variables of ground truth flow fields ( $\mathcal{G}_k(\mathcal{I})$ ) and  $\tilde{u}_k, \tilde{v}_k, \tilde{w}_k, \tilde{p}_k$  be non-dimensionalized flow variables of predicted flow fields ( $G_k(\mathcal{I})$ ). Velocities and pressure are non dimensionalized by  $U_\infty$  and  $\rho U_\infty^2$ , respectively.  $\mathcal{L}_c$  enables networks to learn mass conservation by minimizing the sum of the differences between the incoming and outgoing mass flux distributions in x, y, and z directions as

$$\begin{aligned} \mathcal{L}_c = & n_x \sum_{j=0}^{n_y-1} |(u_{k,(n_x-1,j)} - u_{k,(0,j)}) - (\tilde{u}_{k,(n_x-1,j)} - \tilde{u}_{k,(0,j)})| + \\ & n_y \sum_{i=0}^{n_x-1} |(v_{k,(i,n_y-1)} - v_{k,(i,0)}) - (\tilde{v}_{k,(i,n_y-1)} - \tilde{v}_{k,(i,0)})| + \\ & \sum_{i=0}^{n_x-1} \sum_{j=0}^{n_y-1} |w_{k,(i,j)} - \tilde{w}_{k,(i,j)}| \end{aligned} \quad (7)$$

$\mathcal{L}_{mom}$  enables networks to learn momentum conservation by minimizing the sum of the differences between the incoming and outgoing momentum flux disstributions with additional consideration of pressure at boundaries, as

$$\begin{aligned} \mathcal{L}_{mom} = & n_x \sum_{j=0}^{n_y-1} |(u_{k,(n_x-1,j)}^2 - u_{k,(0,j)}^2) - (\tilde{u}_{k,(n_x-1,j)}^2 - \tilde{u}_{k,(0,j)}^2)| + \\ & n_x \sum_{j=0}^{n_y-1} |(p_{k,(n_x-1,j)} - p_{k,(0,j)}) - (\tilde{p}_{k,(n_x-1,j)} - \tilde{p}_{k,(0,j)})| + \end{aligned}$$

$$\begin{aligned}
& n_y \sum_{i=0}^{n_x-1} \left| (v_{k,(i,n_y-1)}^2 - v_{k,(i,0)}^2) - (\tilde{v}_{k,(i,n_y-1)}^2 - \tilde{v}_{k,(i,0)}^2) \right| + \\
& n_y \sum_{i=0}^{n_x-1} \left| (p_{k,(i,n_y-1)} - p_{k,(i,0)}) - (\tilde{p}_{k,(i,n_y-1)} - \tilde{p}_{k,(i,0)}) \right| + \\
& \sum_{i=0}^{n_x-1} \sum_{j=0}^{n_y-1} |w_{k,(i,j)}^2 - \tilde{w}_{k,(i,j)}^2|. \quad (8)
\end{aligned}$$

$\mathcal{L}_{ke}$  enables networks to learn kinetic energy conservation by comparing the total kinetic energy in a two-dimensional grid.

$$\mathcal{L}_{ke} = \sum_{i=0}^{n_x-1} \sum_{j=0}^{n_y-1} |(u_{k,(i,j)}^2 + v_{k,(i,j)}^2 + w_{k,(i,j)}^2) - (\tilde{u}_{k,(i,j)}^2 + \tilde{v}_{k,(i,j)}^2 + \tilde{w}_{k,(i,j)}^2)| \quad (9)$$

Loss functions  $\mathcal{L}_c$ ,  $\mathcal{L}_{mom}$ , and  $\mathcal{L}_{ke}$  provide explicit prior knowledge of physical conservation laws to networks. These loss functions support the networks to extract features including physical conservation laws in a supervised manner.

$\mathcal{L}_{adv}^G$  is a loss function with a purpose to delude the discriminator model to classify the generated predictions of flow fields to class 1 as

$$\mathcal{L}_{adv}^G = L_{bce}(D_k(G_k(\mathcal{I})), 1), \quad (10)$$

where  $L_{bce}$  is the binary cross entropy loss function defined as

$$L_{bce}(a, b) = -b \log(a) - (1 - b) \log(1 - a), \quad (11)$$

for scalar values a and b between 0 and 1. The loss function  $\mathcal{L}_{adv}^G$  does not

provide any explicit prior knowledge to the network, but provide knowledge in a concealed manner that features of predicted and ground truth flow fields should be indistinguishable. This is the key loss function that provides the network to extract features, which corresponds to physical conservation laws even without providing prior knowledge of the physics, in an unsupervised manner.

The loss function of the discriminator model,

$$\mathcal{L}_{discriminator} = \frac{1}{N} \sum_{k=0}^{N-1} L_{bce}(D_k(\mathcal{G}_k(\mathcal{I})), 1) + L_{bce}(D_k(G_k(\mathcal{I})), 0), \quad (12)$$

is minimized so that the discriminator model appropriately classifies the ground truth flow fields into class 1 and predicted flow fields into class 0. The discriminator model learns concepts in feature space.

## 6. Flow field predictions and evaluations

### 6.1. Error functions for evaluations

Let  $u, v, w, p$  be non-dimensionalized flow variables of the ground truth flow fields ( $\mathcal{G}(\mathcal{I})$ ) and  $\tilde{u}, \tilde{v}, \tilde{w}, \tilde{p}$  be non-dimensionalized flow variables of the generated flow field predictions ( $G(\mathcal{I})$ ). Velocities and pressure are non dimensionalized by  $U_\infty$  and  $\rho U_\infty^2$ , respectively.  $L_2$  error of the prediction is evaluated based on the average difference between the predicted flow vari-

ables as

$$L_2 = \left( \frac{1}{4n_x n_y} \sum_{i=0}^{n_x-1} \sum_{j=0}^{n_y-1} \{ (u_{(i,j)} - \tilde{u}_{(i,j)})^2 + (v_{(i,j)} - \tilde{v}_{(i,j)})^2 + (w_{(i,j)} - \tilde{w}_{(i,j)})^2 + (p_{(i,j)} - \tilde{p}_{(i,j)})^2 \} \right)^{1/2}. \quad (13)$$

$L_\infty$  error of the prediction is evaluated based on the maximum difference between the predicted flow variables as

$$L_\infty = \frac{1}{4} \left( \max_{i,j} (u_{(i,j)} - \tilde{u}_{(i,j)}) + \max_{i,j} (v_{(i,j)} - \tilde{v}_{(i,j)}) + \max_{i,j} (w_{(i,j)} - \tilde{w}_{(i,j)}) + \max_{i,j} (p_{(i,j)} - \tilde{p}_{(i,j)}) \right). \quad (14)$$

Error of mass conservation is evaluated based on the difference between the incoming and outgoing mass flux on  $7D \times 7D$  sized domain boundaries as

$$L_c = \frac{7D}{3n_y} \left| \sum_{j=0}^{n_y-1} (u_{(n_x-1,j)} - u_{(0,j)}) - (\tilde{u}_{(n_x-1,j)} - \tilde{u}_{(0,j)}) \right| + \frac{7D}{3n_x} \left| \sum_{i=0}^{n_x-1} (v_{k,(i,n_y-1)} - v_{k,(i,0)}) - (\tilde{v}_{k,(i,n_y-1)} - \tilde{v}_{k,(i,0)}) \right| + \frac{49D^2}{3n_x n_y} \left| \sum_{i=0}^{n_x-1} \sum_{j=0}^{n_y-1} w_{k,(i,j)} - \tilde{w}_{k,(i,j)} \right|. \quad (15)$$

Error of momentum conservation is evaluated based on the difference between the incoming and outgoing momentum flux and applying pressure

on  $7D \times 7D$  sized domain boundaries as

$$\begin{aligned}
L_{mom} = & \frac{7D}{3n_y} \left( \left| \sum_{j=0}^{n_y-1} (u_{(n_x-1,j)}^2 - u_{(0,j)}^2) - (\tilde{u}_{(n_x-1,j)}^2 - \tilde{u}_{(0,j)}^2) \right| + \right. \\
& \left. \left| \sum_{j=0}^{n_y-1} (p_{(n_x-1,j)} - p_{(0,j)}) - (\tilde{p}_{(n_x-1,j)} - \tilde{p}_{(0,j)}) \right| \right) + \\
& \frac{7D}{3n_x} \left( \left| \sum_{i=0}^{n_x-1} (v_{(i,n_y-1)}^2 - v_{(i,0)}^2) - (\tilde{v}_{(i,n_y-1)}^2 - \tilde{v}_{(i,0)}^2) \right| + \right. \\
& \left. \left| \sum_{i=0}^{n_x-1} (p_{(i,n_y-1)} - p_{(i,0)}) - (\tilde{p}_{(i,n_y-1)} - \tilde{p}_{(i,0)}) \right| \right) + \\
& \frac{49D^2}{3n_x n_y} \left| \sum_{i=0}^{n_x-1} \sum_{j=0}^{n_y-1} w_{(i,j)}^2 - \tilde{w}_{(i,j)}^2 \right|. \quad (16)
\end{aligned}$$

Error of kinetic energy conservation is evaluated based on the difference between the kinetic energy inside a  $7D \times 7D$  sized domain as

$$L_{ke} = \frac{49D^2}{n_x n_y} \left| \sum_{i=0}^{n_x-1} \sum_{j=0}^{n_y-1} (u_{(i,j)}^2 + v_{(i,j)}^2 + w_{(i,j)}^2) - (\tilde{u}_{(i,j)}^2 + \tilde{v}_{(i,j)}^2 + \tilde{w}_{(i,j)}^2) \right|. \quad (17)$$

## 6.2. Flow field predictions without prior knowledge of conservation laws

In this section flow fields at  $Re_D = 100, 200, 300$  and  $400$  are trained with a generator model (configuration of  $GM_{20}$  and number set  $N_{64}$ ) without prior knowledge of conservation laws. Therefore, parameters of loss functions of  $\lambda_{l2} = \lambda_{gdl} = 0.5$  and  $\lambda_c = \lambda_{mom} = \lambda_{ke} = \lambda_{adv} = 0.0$  are applied. Qualitative flow field predictions at  $Re_D = 500$  and  $3000$  from the network are shown in figure 5 and 6. Predictions of qualitative flow fields from the network show

good agreements with the ground truth flow fields even the domain and grid sizes for predictions ( $7D \times 7D$  and  $250 \times 250$ ) are larger than the domain and grid sizes used in training ( $0.896D \times 0.896D$  and  $32 \times 32$ ). This is because the fully convolutional architecture in the generator model learns to extract low dimensional representations of local flow features due to multi-scale CNNs. However, dissipations of small-scale flow structures are observed in the flow field prediction at  $Re_D = 3000$ , as the generator has not been trained with flow fields containing small-scale flow structures.

Flow field predictions after time-step interval larger than  $\delta t$  are predicted recursively by utilizing flow field predictions from the previous time-step as a part of input. The recursively predicted flow fields at  $Re_D = 3000$  are shown in figure 7. Difference between flow fields increases as the recursive prediction step increases as errors from the previous prediction is propagated to the next time-step prediction. Dissipation of small-scale flow structures and unphysical large-scale flow structures at region between the front stagnation and separation and wake are observed as the time-step increases; however, large-scale flow structures from vortex shedding are reasonably predicted. Quantitative errors of flow field predictions are compared with other deep learning networks in following sections.

### *6.3. Flow field predictions with prior knowledge of physical conservation laws*

Effects of providing prior knowledge of physical conservation laws are evaluated by training flow fields using a generator model with physical loss

functions. The parameters of the loss functions are  $\lambda_{l2} = \lambda_{gdl} = \lambda_c = \lambda_{mom} = \lambda_{ke} = 0.2$  and  $\lambda_{adv} = 0.0$ ; the physical loss functions are applied and adversarial training is not applied. Errors of flow field predictions from generators (configuration of  $GM_{20}$  and number set  $N_{64}$ ) with and without physical loss functions are quantitatively compared in figure 8. Flow field predictions with and without physical loss functions show similar levels in  $L_2$  and  $L_\infty$  errors, as both flow field predictions utilize loss functions of  $\mathcal{L}_2$  and  $\mathcal{L}_{gdl}$ , which minimizes the difference between predicted and ground truth flow fields. However, drop of errors of  $L_c$ ,  $L_{mom}$ , and  $L_{ke}$  are observed when physical loss functions are applied. Therefore, the observation implies that the applied physical loss functions assist the supervised feature extraction based network to learn physical conservation laws by providing the prior knowledge of the conservation laws. The prior knowledge of the conservation laws trains the deep learning network to extract low dimensional flow features that not only minimizes the difference between the predicted and ground truth flow fields, but also minimizes the discrepancy of mass, momentum, and kinetic energy between the predicted and ground truth flow fields.

Qualitative predictions of flow fields at  $Re_D = 500$  and 3000 are shown in figure 9 and 10, respectively, while recursively predicted flow fields at  $Re_D = 3000$  are compared with the ground truth flow fields in figure 11. The qualitative comparison is conducted with a generator model with configuration of  $GM_{20}$  and number set  $N_{64}$ . Large-scale flow structures of predicted flow fields after a single time-step ( $\delta t$ ) at  $Re_D = 500$  and 3000 agree well

with ground truth data, while dissipations of small-scale flow structures are observed in the flow field prediction at  $Re_D = 3000$ . These qualitative predictions of flow fields do not show big difference with flow field predictions without prior knowledge of conservation laws. In the case of recursive prediction, small-scale flow structures are dissipated and large-scale flow structures are being unphysical as the time-step increases; also, pressure with high gradient in cross-flow direction at wake is observed, which is not observed in results from prediction using the generator model without prior knowledge of physical conservation laws. However, large-scale flow structures from vortex shedding are reasonably predicted. The errors from recursive prediction increase first-orderly (see figure 12), but  $L_{ke}$  shows a drop at recursive flow field prediction at  $2\delta t$ . This is because  $L_{ke}$  is an error criterion which is dominated by macro flow fields in a domain; therefore,  $L_{ke}$  is not crucially influenced by the dissipation of small-scale flow motions.

The effects of number of weight layers and number sets of generator models on flow prediction at  $Re_D = 3000$  are shown in figure 13 and 14, respectively. Flow prediction at  $Re_D = 3000$  with number set  $N_{32}$  shows minimum error of  $L_2, L_\infty$ , and  $L_{mom}$ , while  $N_{64}$  shows minimum error of  $L_c$  and  $L_{ke}$ . The generator model  $GM_{16}$  shows minimum error of  $L_2$ , while  $GM_{18}$  shows minimum error of  $L_c, L_{mom}$ . The largest generator model,  $GM_{20}$ , shows minimum error of  $L_\infty$ . No clear trends in errors respect to network sizes are observed.

#### 6.4. Flow field predictions with unsupervised feature extraction

Effects of unsupervised feature extraction are analyzed by utilizing a generator model with configuration of  $GM_{20}$  and discriminator model with number set  $N_{64}$ . The effect of adversarial training is analyzed by tuning weight parameters of loss functions as table 4, while the corresponding errors are compared in figure 15. High percentage of adversarial training influences the networks to extract low dimensional features in an unsupervised manner. These unsupervised extraction of low dimensional features supports networks to discover prior knowledge of data, but it also may cause unstable or inefficient training if it is too high. In our case, the best overall performance of conservation errors ( $L_c$ ,  $L_{mom}$ , and  $L_{ke}$ ) is achieved with 7.5% adversarial training, while the best performance of  $L_2$  and  $L_\infty$  errors is obtained with no adversarial training; the errors are evaluated on flow field predictions at  $Re_D = 3000$ .

Errors of flow field predictions at  $Re_D = 500$  and 3000 with and without adversarial training are quantitatively compared in figure 16. 7.5% of adversarial training is applied. Similar to flow field predictions with prior knowledge of physical conservation laws, comparable levels in  $L_2$  and  $L_\infty$  errors and decreases of errors of  $L_c$ ,  $L_{mom}$ , and  $L_{ke}$  are observed. The observation implies that the discriminator model extracts features including physical conservation laws and learns the conservation laws by minimizing the discrepancy between the predicted and ground truth flow fields in feature space. Therefore, unsupervised feature extraction shows potentials to

discover and learn prior knowledge that is uncovered in data. Qualitative predictions of flow fields at  $Re_D = 500$  and  $3000$  from the network are shown in figure 17 and 18, respectively. Flow field prediction results after a single time-step ( $\delta t$ ) at  $Re_D = 500$  and  $Re_D = 3000$  show good agreement of large-scale flow fields with ground truth data, while dissipations of small-scale flow structures are observed in the flow field prediction at  $Re_D = 3000$ . These qualitative predictions do not show big difference with flow field predictions with and without prior knowledge of conservation laws.

Recursively predicted flow fields at  $Re_D = 3000$  are compared with the ground truth flow fields in figure 19; the corresponding errors from recursive prediction increase first-orderly (see figure 20). Dissipation of small-scale flow structures and unphysical large-scale flow structures are observed as the time-step increases. Pressure with high gradient in cross-flow direction at wake is observed, which is consistent with results from prediction using the generator model with prior knowledge of physical conservation laws. Also, Large-scale flow structures from vortex shedding are reasonably predicted. The qualitative results are consistent with results from generator model with prior knowledge of physical conservation laws, which also implies adversarial training extracts features including physical conservation laws.

Tendencies of errors of  $L_2$ ,  $L_\infty$ ,  $L_c$ , and  $L_{mom}$  are similar to the errors from flow field predictions with prior knowledge of conservation laws, however  $L_{ke}$  in unsupervised feature extraction shows additional drop at prediction at  $3\delta t$ .

The effects of number of weight layers and number sets of generator models on flow field prediction are shown in figure 21 and 22, respectively. Flow prediction at  $Re_D = 3000$  with number set  $N_{32}$  shows minimum error of  $L_2$  and  $N_{64}$  shows minimum error of  $L_\infty$ ,  $L_c$ ,  $L_{mom}$  and  $L_{ke}$ . The generator model  $GM_{16}$  shows minimum error of  $L_2$ ,  $L_\infty$ , and  $L_{mom}$ , while the largest generator model,  $GM_{20}$ , shows minimum error of  $L_c$ , and  $L_{ke}$ . The largest network is observed to learn mass and kinetic energy conservations the best, while  $L_2$  difference is learned better in smaller networks.

#### 6.5. Flow field predictions with physical loss functions and adversarial training

Errors from a network with both physical loss functions and adversarial training are compared with errors from networks with physical loss functions or adversarial training (see figure 23). Parameters of loss functions for the network with physical loss functions and adversarial training are  $\lambda_{l2} = \lambda_{gdl} = \lambda_c = \lambda_{mom} = \lambda_{ke} = 0.185$  and  $\lambda_{adv} = 0.075$ . A generator model with configuration of  $GM_{20}$  and number set  $N_{64}$  and discriminator model with number set  $N_{64}$  is employed. Utilization of both physical loss functions and adversarial training does not enhance the performance of flow field predictions, since physical loss functions and adversarial training both extract low dimensional features including physical conservation laws.

## 7. Conclusions

Flow fields at future occasions around a circular cylinder at  $Re_D = 500$  and 3000, which are not in the training dataset, were successfully predicted using deep learning, which had been trained using flow field datasets produced by numerical simulations at  $Re_D = 100, 200, 300$  and 400. The utilized deep learning networks provide good predictions of flow fields after a single time-step even on a larger domain than training because the networks learns to extract features based on the underlying physics by multi-scale CNNs. However, in the case of recursive prediction, dissipation of small-scale flow structures and unphysical large-scale flow structures appear as the prediction time-step increases, even large-scale flow structures from vortex shedding are reasonably predicted. The proposed physical loss functions and adversarial training are observed to support the network to learn physical conservation laws. Especially, observations from adversarial training implies that a discriminator model is able to learn physical conservation laws even without prior knowledge of the conservation laws. This is because adversarial training extracts features containing physical conservation laws in an unsupervised manner. Thus, unsupervised feature extraction can be applied to many practical data, which lack information of the full underlying physics, to extract undiscovered prior knowledge in data.

## 8. Acknowledgements

This work was supported by Samsung Research Funding Center of Samsung Electronics under Project Number SRFC-TB1703-01.

## References

- [1] P. Dalin, N. Pertsev, S. Frandsen, O. Hansen, H. Andersen, A. Dubietis, R. Balciunas, A case study of the evolution of a Kelvin–Helmholtz wave and turbulence in noctilucent clouds, *Journal of Atmospheric and Solar-Terrestrial Physics* 72 (2010) 1129–1138.
- [2] E. Berger, R. Wille, Periodic flow phenomena, *Annual Review of Fluid Mechanics* 4 (1972) 313–340.
- [3] P. S. Marcus, Numerical simulation of Jupiter’s great red spot, *Nature* 331 (1988) 693–696.
- [4] P. Freymuth, On transition in a separated laminar boundary layer, *Journal of Fluid Mechanics* 25 (1966) 683–704.
- [5] R. Ruderich, H. Fernholz, An experimental investigation of a turbulent shear flow with separation, reverse flow, and reattachment, *Journal of Fluid Mechanics* 163 (1986) 283–322.
- [6] X. Wu, P. Moin, Direct numerical simulation of turbulence in a nominally zero-pressure-gradient flat-plate boundary layer, *Journal of Fluid Mechanics* 630 (2009) 5–41.

- [7] A. Babucke, M. Kloker, U. Rist, DNS of a plane mixing layer for the investigation of sound generation mechanisms, *Computers & Fluids* 37 (2008) 360–368.
- [8] L. Sirovich, Turbulence and the dynamics of coherent structures part I: coherent structures, *Quarterly of Applied Mathematics* 45 (1987) 561–571.
- [9] P. J. Schmid, Dynamic mode decomposition of numerical and experimental data, *Journal of Fluid Mechanics* 656 (2010) 5–28.
- [10] I. Mezić, Analysis of fluid flows via spectral properties of the Koopman operator, *Annual Review of Fluid Mechanics* 45 (2013) 357–378.
- [11] T. Y. Wu, Fish swimming and bird/insect flight, *Annual Review of Fluid Mechanics* 43 (2011) 25–58.
- [12] Y. Yonehara, Y. Goto, K. Yoda, Y. Watanuki, L. C. Young, H. Weimerskirch, C.-A. Bost, K. Sato, Flight paths of seabirds soaring over the ocean surface enable measurement of fine-scale wind speed and direction, *Proceedings of the National Academy of Sciences* 113 (2016) 9039–9044.
- [13] D. E. Rumelhart, G. E. Hinton, R. J. Williams, Learning representations by back-propagating errors, *Nature* 323 (1986) 533.
- [14] C. Lee, J. Kim, D. Babcock, R. Goodman, Application of neural networks to turbulence control for drag reduction, *Physics of Fluids* 9 (1997) 1740–1747.

- [15] J. Pruvost, J. Legrand, P. Legentilhomme, Three-dimensional swirl flow velocity-field reconstruction using a neural network with radial basis functions, *Journal of Fluids Engineering* 123 (2001) 920–927.
- [16] Y. Chen, G. Kopp, D. Surry, Interpolation of wind-induced pressure time series with an artificial neural network, *Journal of Wind Engineering and Industrial Aerodynamics* 90 (2002) 589–615.
- [17] M. Milano, P. Koumoutsakos, Neural network modeling for near wall turbulent flow, *Journal of Computational Physics* 182 (2002) 1–26.
- [18] F. Sarghini, G. De Felice, S. Santini, Neural networks based subgrid scale modeling in large eddy simulations, *Computers & Fluids* 32 (2003) 97–108.
- [19] A. Krizhevsky, I. Sutskever, G. E. Hinton, Imagenet classification with deep convolutional neural networks, in: *Advances in Neural Information Processing Systems*, 2012, pp. 1097–1105.
- [20] B. Tracey, K. Duraisamy, J. Alonso, A machine learning strategy to assist turbulence model development, *AIAA Paper 1287* (2015) 2015.
- [21] Z. J. Zhang, K. Duraisamy, Machine learning methods for data-driven turbulence modeling, *AIAA 2460* (2015) 2015.
- [22] J. Ling, A. Kurzawski, J. Templeton, Reynolds averaged turbulence modelling using deep neural networks with embedded invariance, *Journal of Fluid Mechanics* 807 (2016) 155–166.

- [23] X. Guo, W. Li, F. Iorio, Convolutional neural networks for steady flow approximation, in: Proceedings of the 22nd ACM SIGKDD International Conference on Knowledge Discovery and Data Mining, ACM, 2016, pp. 481–490.
- [24] T. P. Miyanawala, R. K. Jaiman, An efficient deep learning technique for the Navier-Stokes equations: Application to unsteady wake flow dynamics, arXiv preprint arXiv:1710.09099 (2017).
- [25] A. Radford, L. Metz, S. Chintala, Unsupervised representation learning with deep convolutional generative adversarial networks, arXiv preprint arXiv:1511.06434 (2015).
- [26] E. L. Denton, S. Chintala, R. Fergus, et al., Deep generative image models using a Laplacian pyramid of adversarial networks, in: Advances in Neural Information Processing Systems, 2015, pp. 1486–1494.
- [27] A. v. d. Oord, N. Kalchbrenner, K. Kavukcuoglu, Pixel recurrent neural networks, arXiv preprint arXiv:1601.06759 (2016).
- [28] A. van den Oord, N. Kalchbrenner, L. Espeholt, O. Vinyals, A. Graves, et al., Conditional image generation with PixelCNN decoders, in: Advances in Neural Information Processing Systems, 2016, pp. 4790–4798.
- [29] N. Srivastava, E. Mansimov, R. Salakhudinov, Unsupervised learning of video representations using LSTMs, in: International Conference on Machine Learning, 2015, pp. 843–852.

- [30] M. Ranzato, A. Szlam, J. Bruna, M. Mathieu, R. Collobert, S. Chopra, Video (language) modeling: a baseline for generative models of natural videos, arXiv preprint arXiv:1412.6604 (2014).
- [31] M. Mathieu, C. Couprie, Y. LeCun, Deep multi-scale video prediction beyond mean square error, arXiv preprint arXiv:1511.05440 (2015).
- [32] I. Goodfellow, J. Pouget-Abadie, M. Mirza, B. Xu, D. Warde-Farley, S. Ozair, A. Courville, Y. Bengio, Generative adversarial nets, in: Advances in Neural Information Processing Systems, 2014, pp. 2672–2680.
- [33] D. You, F. Ham, P. Moin, Discrete conservation principles in large-eddy simulation with application to separation control over an airfoil, Physics of Fluids 20 (2008) 101515.
- [34] D. P. Kingma, J. Ba, Adam: A method for stochastic optimization, CoRR abs/1412.6980 (2014). URL: <http://arxiv.org/abs/1412.6980>. arXiv:1412.6980.

## List of Tables

1	Number sets used in the generator and discriminator models. .	42
2	Configurations of generator models. . . . .	42
3	Configuration of the discriminator model. . . . .	43
4	Weight parameters of loss function for calculating adversarial training effects. $\lambda_c$ , $\lambda_{mom}$ , and $\lambda_{ke}$ are zero. . . . .	43

## List of Figures

- 1 The computational domain for numerical simulations.  $N$  denotes the number of mesh points, where  $N_{x_1} = 20$ ,  $N_{x_2} = 30$ ,  $N_{x_3} = 50$ ,  $N_{x_4} = 50$ ,  $N_{y_1} = 30$ ,  $N_{y_2} = 30$ ,  $N_{y_3} = 80$ , and  $N_\theta = 150$ . The domain size and number of mesh points in the spanwise direction are  $6D$  and  $96$ . . . . . 44
- 2 (a) Instantaneous flow variables of  $u/U_\infty, v/U_\infty, w/U_\infty, p/\rho U_\infty^2$  ( $250 \times 250$  sized grid and  $7D \times 7D$  sized domain). (b) The procedure of subsampling five consecutive flow fields to an input ( $\mathcal{I}$ ) and ground truth ( $\mathcal{G}(\mathcal{I})$ ) of a training sample on a  $32 \times 32$  sized grid and  $0.896 \times 0.896$  sized domain. . . . . 45
- 3 Schematic diagram of generator models.  $\mathcal{I}$  is the set of input flow fields and  $\mathcal{I}_k$  denotes interpolated input flow fields on a  $1/(2^k \times 2^k)$  smaller scale grid, while domain sizes are identical.  $G_k$  indicates a generative CNN which is fed with input  $\mathcal{I}_k$ , while  $G_k(\mathcal{I})$  indicates the set of generated predictions of flow fields from generative CNN  $G_k$ .  $R_k$  indicates the rescale operator, which upscales the grid size twice in both height and width. . . . . 46

4	Schematic diagram of the discriminator model. $D_k$ indicates the discriminative network which is fed with $G_k(\mathcal{I})$ and $\mathcal{G}_k(\mathcal{I})$ . $G_k(\mathcal{I})$ indicates the set of generated predictions of flow fields from generative CNN $G_k$ , while $\mathcal{G}_k(\mathcal{I})$ indicates the set of ground truth flow fields. . . . .	46
5	Comparison between the predicted and ground truth flow fields at test data ( $Re_D = 500$ ) using a generator model ( $GM_{20}$ and $N_{64}$ ) based on supervised feature extraction without prior knowledge of physical conservation laws: (a-d) are the input sets of flow fields, where (e) and (f) are the predicted and ground truth flow fields. Each group of two rows from top to bottom indicate $u/U_\infty$ , $v/U_\infty$ , $w/U_\infty$ , and $p/\rho U_\infty^2$ . 15 contours for $u/U_\infty$ , $v/U_\infty$ , and $w/U_\infty$ are ranged from -0.5 to 1.0, -0.7 to 0.7, and -0.5 to 0.5. 20 contours for $p/\rho U_\infty^2$ are ranged from -1.0 to 0.4. Solid line — and dotted line -- indicate positive and negative levels, respectively. The time-step interval between flow fields is $\delta t = 0.01$ . . . . .	47

6	Comparison between the predicted and ground truth flow fields at test data ( $Re_D = 3000$ ) using a generator model ( $GM_{20}$ and $N_{64}$ ) based on supervised feature extraction without prior knowledge of physical conservation laws: (a-d) are the input sets of flow fields, where (e) and (f) are the predicted and ground truth flow fields. Each group of two rows from top to bottom indicate $u/U_\infty$ , $v/U_\infty$ , $w/U_\infty$ , and $p/\rho U_\infty^2$ . 15 contours for $u/U_\infty$ , $v/U_\infty$ , and $w/U_\infty$ are ranged from -0.5 to 1.0, -0.7 to 0.7, and -0.5 to 0.5. 20 contours for $p/\rho U_\infty^2$ are ranged from -1.0 to 0.4. Solid line — and dotted line -- indicate positive and negative levels, respectively. The time-step interval between flow fields is $\delta t = 0.01$ . . . . .	48
---	--	----

7      Comparison between the recursively predicted flow fields and ground truth flow fields of flow variables at  $Re_D = 3000$  using a generator model ( $GM_{20}$  and  $N_{64}$ ) based on supervised feature extraction without prior knowledge of physical conservation laws: (a)  $u/U_\infty$ , (b)  $v/U_\infty$ , (c)  $w/U_\infty$ , (d)  $p/\rho U_\infty^2$ . The first and second rows show the recursively predicted and ground truth flow fields after  $\delta t$ ,  $5\delta t$ ,  $10\delta t$  (from left to right). 15 contours for  $u/U_\infty$ ,  $v/U_\infty$ , and  $w/U_\infty$  are ranged from -0.5 to 1.0, -0.7 to 0.7, and -0.5 to 0.5. 20 contours for  $p/\rho U_\infty^2$  are ranged from -1.0 to 0.4. Solid line — and dotted line -- indicate positive and negative levels, respectively. The time-step interval between input flow fields is  $\delta t = 0.01$ . . . . . 49

- 8 Comparison between errors from generator models with and without prior knowledge of physical conservation laws: (a) and (b) are the  $L_2$  and  $L_\infty$  errors; (c), (d), and (e) are the  $L_c$ ,  $L_{mom}$ , and  $L_{ke}$  errors.  $\circ$  denotes errors from a generator model based on supervised feature extraction without prior knowledge of physical conservation laws (configuration of  $GM_{20}$ , number set  $N_{64}$ ,  $\lambda_{l2} = \lambda_{gdl} = 0.5$  and  $\lambda_{adv} = \lambda_c = \lambda_{mom} = \lambda_{ke} = 0.0$ );  $\square$  denotes errors from a generator model based on supervised feature extraction with prior knowledge of physical conservation laws (configuration of  $GM_{20}$ , number set  $N_{64}$ ,  $\lambda_{l2} = \lambda_{gdl} = \lambda_c = \lambda_{mom} = \lambda_{ke} = 0.2$  and  $\lambda_{adv} = 0.0$ ). The errorbars represents the standard deviation. . . . . 50
- 9 Comparison between the predicted and ground truth flow fields at test data ( $Re_D = 500$ ) using a generator model ( $GM_{20}$  and  $N_{64}$ ) with prior knowledge of physical conservation laws: (a-d) are the input sets of flow fields, where (e) and (f) are the predicted and ground truth flow fields. 15 contours for  $u/U_\infty$ ,  $v/U_\infty$ , and  $w/U_\infty$  are ranged from -0.5 to 1.0, -0.7 to 0.7, and -0.5 to 0.5. 20 contours for  $p/\rho U_\infty^2$  are ranged from -1.0 to 0.4. Solid line — and dotted line -- indicate positive and negative levels, respectively. The time-step interval between flow fields is  $\delta t = 0.01$ . . . . . 51

- 10 Comparison between the predicted and ground truth flow fields at test data ( $Re_D = 3000$ ) using a generator model ( $GM_{20}$  and  $N_{64}$ ) with prior knowledge of physical conservation laws: (a-d) are the input sets of flow fields, where (e) and (f) are the predicted and ground truth flow fields. 15 contours for  $u/U_\infty$ ,  $v/U_\infty$ , and  $w/U_\infty$  are ranged from -0.5 to 1.0, -0.7 to 0.7, and -0.5 to 0.5. 20 contours for  $p/\rho U_\infty^2$  are ranged from -1.0 to 0.4. Solid line — and dotted line -- indicate positive and negative levels, respectively. The time-step interval between flow fields is  $\delta t = 0.01$ . . . . . 52
- 11 Comparison between the recursively predicted flow fields and ground truth flow fields of flow variables at  $Re_D = 3000$  using a generator model ( $GM_{20}$  and  $N_{64}$ ) with prior knowledge of physical conservation laws: (a)  $u/U_\infty$ , (b)  $v/U_\infty$ , (c)  $w/U_\infty$ , (d)  $p/\rho U_\infty^2$ . The first and second rows show the recursively predicted and ground truth flow fields after  $\delta t$ ,  $5\delta t$ ,  $10\delta t$  (from left to right). 15 contours for  $u/U_\infty$ ,  $v/U_\infty$ , and  $w/U_\infty$  are ranged from -0.5 to 1.0, -0.7 to 0.7, and -0.5 to 0.5. 20 contours for  $p/\rho U_\infty^2$  are ranged from -1.0 to 0.4. Solid line — and dotted line -- indicate positive and negative levels, respectively. The time-step interval between input flow fields is  $\delta t = 0.01$ . . . . 53

12	Flow prediction errors at $Re_D = 3000$ respect to recursive prediction step using a generator model ( $GM_{20}$ and $N_{64}$ ) with prior knowledge of physical conservation laws: (a) and (b) are the $L_2$ and $L_\infty$ errors; (c), (d), and (e) are the $L_c$ , $L_{mom}$ , and $L_{ke}$ errors. . . . .	54
13	Flow prediction errors at $Re_D = 3000$ respect to three cases of number set using generator models with prior knowledge of physical conservation laws: (a) and (b) are the $L_2$ and $L_\infty$ errors; (c), (d), and (e) are the $L_c$ , $L_{mom}$ , and $L_{ke}$ errors. . . .	55
14	Flow prediction errors at $Re_D = 3000$ respect to three cases of generator configuration with prior knowledge of physical conservation laws: (a) and (b) are the $L_2$ and $L_\infty$ errors; (c), (d), and (e) are the $L_c$ , $L_{mom}$ , and $L_{ke}$ errors. . . . .	56
15	Flow prediction errors at $Re_D = 3000$ respect to adversarial training percentage using a generator model ( $GM_{20}$ and $N_{64}$ ): (a) and (b) are the $L_2$ and $L_\infty$ errors; (c), (d), and (e) are the $L_c$ , $L_{mom}$ , and $L_{ke}$ errors. . . . .	57

- 16 Comparison between errors from generator models with and without unsupervised feature extraction: (a) and (b) are the  $L_2$  and  $L_\infty$  errors; (c), (d), and (e) are the  $L_c$ ,  $L_{mom}$ , and  $L_{ke}$  errors.  $\circ$  denotes errors from a generator model based on supervised feature extraction without prior knowledge of physical conservation laws (configuration of  $GM_{20}$ , number set  $N_{64}$ ,  $\lambda_{l2} = \lambda_{gdl} = 0.5$  and  $\lambda_{adv} = \lambda_c = \lambda_{mom} = \lambda_{ke} = 0.0$ );  $\square$  denotes errors from a generator model associated with unsupervised feature extraction (configuration of  $GM_{20}$ , number set  $N_{64}$ ,  $\lambda_{l2} = \lambda_{gdl} = 0.4625$ ,  $\lambda_{adv} = 0.075$ , and  $\lambda_c = \lambda_{mom} = \lambda_{ke} = 0.0$ ). The errorbars represents the standard deviation. . 58
- 17 Comparison between the predicted and ground truth flow fields at test data ( $Re_D = 500$ ) using a generator model ( $GM_{20}$  and  $N_{64}$ ) associated with unsupervised feature extraction: (a-d) are the input sets of flow fields, where (e) and (f) are the predicted and ground truth flow fields. 15 contours for  $u/U_\infty$ ,  $v/U_\infty$ , and  $w/U_\infty$  are ranged from -0.5 to 1.0, -0.7 to 0.7, and -0.5 to 0.5. 20 contours for  $p/\rho U_\infty^2$  are ranged from -1.0 to 0.4. Solid line — and dotted line -- indicate positive and negative levels, respectively. The time-step interval between flow fields is  $\delta t = 0.01$ . . . . . 59

- 18 Comparison between the predicted and ground truth flow fields at test data ( $Re_D = 3000$ ) using a generator model ( $GM_{20}$  and  $N_{64}$ ) associated with unsupervised feature extraction: (a-d) are the input sets of flow fields, where (e) and (f) are the predicted and ground truth flow fields. 15 contours for  $u/U_\infty$ ,  $v/U_\infty$ , and  $w/U_\infty$  are ranged from -0.5 to 1.0, -0.7 to 0.7, and -0.5 to 0.5. 20 contours for  $p/\rho U_\infty^2$  are ranged from -1.0 to 0.4. Solid line — and dotted line -- indicate positive and negative levels, respectively. The time-step interval between flow fields is  $\delta t = 0.01$ . . . . . 60
- 19 Comparison between the recursively predicted flow fields and ground truth flow fields of flow variables at  $Re_D = 3000$  using a generator model ( $GM_{20}$  and  $N_{64}$ ) associated with unsupervised feature extraction: (a)  $u/U_\infty$ , (b)  $v/U_\infty$ , (c)  $w/U_\infty$ , (d)  $p/\rho U_\infty^2$ . The first and second rows show the recursively predicted and ground truth flow fields after  $\delta t$ ,  $5\delta t$ ,  $10\delta t$  (from left to right). 15 contours for  $u/U_\infty$ ,  $v/U_\infty$ , and  $w/U_\infty$  are ranged from -0.5 to 1.0, -0.7 to 0.7, and -0.5 to 0.5. 20 contours for  $p/\rho U_\infty^2$  are ranged from -1.0 to 0.4. Solid line — and dotted line -- indicate positive and negative levels, respectively. The time-step interval between input flow fields is  $\delta t = 0.01$ . . 61

20	Flow prediction errors at $Re_D = 3000$ respect to recursive prediction step using a generator model ( $GM_{20}$ and $N_{64}$ ) associated with unsupervised feature extraction: (a) and (b) are the $L_2$ and $L_\infty$ errors; (c), (d), and (e) are the $L_c$ , $L_{mom}$ , and $L_{ke}$ errors. . . . .	62
21	Flow prediction errors at $Re_D = 3000$ respect to three cases of number set using generator models associated with unsupervised feature extraction: (a) and (b) are the $L_2$ and $L_\infty$ errors; (c), (d), and (e) are the $L_c$ , $L_{mom}$ , and $L_{ke}$ errors. . . .	63
22	Flow prediction errors at $Re_D = 3000$ respect to three cases of generator configuration associated with unsupervised feature extraction: (a) and (b) are the $L_2$ and $L_\infty$ errors; (c), (d), and (e) are the $L_c$ , $L_{mom}$ , and $L_{ke}$ errors. . . . .	64

23	Comparison between errors from networks associated with unsupervised feature extraction with and without prior knowledge of physical conservation laws: (a) and (b) are the $L_2$ and $L_\infty$ errors; (c), (d), and (e) are the $L_c$ , $L_{mom}$ , and $L_{ke}$ errors. $\circ$ denotes errors from a generator model with prior knowledge of physical conservation laws (configuration of $GM_{20}$ , number set $N_{64}$ , $\lambda_{l2} = \lambda_{gdl} = \lambda_c = \lambda_{mom} = \lambda_{ke} = 0.2$ and $\lambda_{adv} = 0.0$ ); $\square$ denotes errors from a generator model associated with unsupervised feature extraction (configuration of $GM_{20}$ , number set $N_{64}$ , $\lambda_{l2} = \lambda_{gdl} = 0.4625$ , $\lambda_{adv} = 0.075$ , and $\lambda_c = \lambda_{mom} = \lambda_{ke} = 0.0$ ); $\triangle$ denotes errors from a generator model with both unsupervised feature extraction and prior knowledge of physical conservation laws (configuration of $GM_{20}$ , number set $N_{64}$ , $\lambda_{l2} = \lambda_{gdl} = \lambda_c = \lambda_{mom} = \lambda_{ke} = 0.185$ and $\lambda_{adv} = 0.075$ ). The errorbars represents the standard deviation.	65
----	---	----

Number set	$\mathcal{N}_1$	$\mathcal{N}_2$	$\mathcal{N}_3$	$\mathcal{N}_4$	$\mathcal{N}_5$
$N_{16}$	16	32	64	128	256
$N_{32}$	32	64	128	256	512
$N_{64}$	64	128	256	512	1024

Table 1: Number sets used in the generator and discriminator models.

Configuration	Generator	Feature map sizes						Kernel sizes					
$GM_{16}$	$G_3$	16	$\mathcal{N}_2$	$\mathcal{N}_2$	4			3	3	3			
	$G_2$	20	$\mathcal{N}_2$	$\mathcal{N}_2$	4			5	3	5			
	$G_1$	20	$\mathcal{N}_2$	$\mathcal{N}_3$	$\mathcal{N}_3$	$\mathcal{N}_2$	4	5	3	3	3	5	
	$G_0$	20	$\mathcal{N}_2$	$\mathcal{N}_3$	$\mathcal{N}_3$	$\mathcal{N}_2$	4	7	5	5	5	7	
$GM_{18}$	$G_3$	16	$\mathcal{N}_2$	$\mathcal{N}_3$	$\mathcal{N}_2$	4			3	3	3	3	
	$G_2$	20	$\mathcal{N}_2$	$\mathcal{N}_3$	$\mathcal{N}_2$	4			5	3	3	5	
	$G_1$	20	$\mathcal{N}_2$	$\mathcal{N}_3$	$\mathcal{N}_3$	$\mathcal{N}_2$	4	5	3	3	3	5	
	$G_0$	20	$\mathcal{N}_2$	$\mathcal{N}_3$	$\mathcal{N}_3$	$\mathcal{N}_2$	4	7	5	5	5	7	
$GM_{20}$	$G_3$	16	$\mathcal{N}_2$	$\mathcal{N}_3$	$\mathcal{N}_2$	4			3	3	3	3	
	$G_2$	20	$\mathcal{N}_2$	$\mathcal{N}_3$	$\mathcal{N}_2$	4			5	3	3	5	
	$G_1$	20	$\mathcal{N}_2$	$\mathcal{N}_3$	$\mathcal{N}_4$	$\mathcal{N}_3$	$\mathcal{N}_2$	4	5	3	3	3	5
	$G_0$	20	$\mathcal{N}_2$	$\mathcal{N}_3$	$\mathcal{N}_4$	$\mathcal{N}_3$	$\mathcal{N}_2$	4	7	5	5	5	7

Table 2: Configurations of generator models.

Layer type	Discriminator	Feature map/layer sizes	Kernel sizes
CNN	$D_3$	4 $\mathcal{N}_1$	3
	$D_2$	4 $\mathcal{N}_1$ $\mathcal{N}_2$ $\mathcal{N}_2$	3 3 3
	$D_1$	4 $\mathcal{N}_2$ $\mathcal{N}_3$ $\mathcal{N}_3$	5 5 5
	$D_0$	4 $\mathcal{N}_2$ $\mathcal{N}_3$ $\mathcal{N}_4$ $\mathcal{N}_2$	7 7 5 5
FC	$D_3$	$\mathcal{N}_4$ $\mathcal{N}_3$ 1	
	$D_2$	$\mathcal{N}_5$ $\mathcal{N}_4$ 1	
	$D_1$	$\mathcal{N}_5$ $\mathcal{N}_4$ 1	
	$D_0$	$\mathcal{N}_5$ $\mathcal{N}_4$ 1	

Table 3: Configuration of the discriminator model.

Calculations	$\lambda_{l2}$	$\lambda_{gdl}$	$\lambda_{adv}$
0% adv	0.5	0.5	0.0
2.5% adv	0.4875	0.4875	0.025
5% adv	0.475	0.475	0.05
7.5% adv	0.4625	0.4625	0.075
10% adv	0.45	0.45	0.1

Table 4: Weight parameters of loss function for calculating adversarial training effects.  $\lambda_c$ ,  $\lambda_{mom}$ , and  $\lambda_{ke}$  are zero.

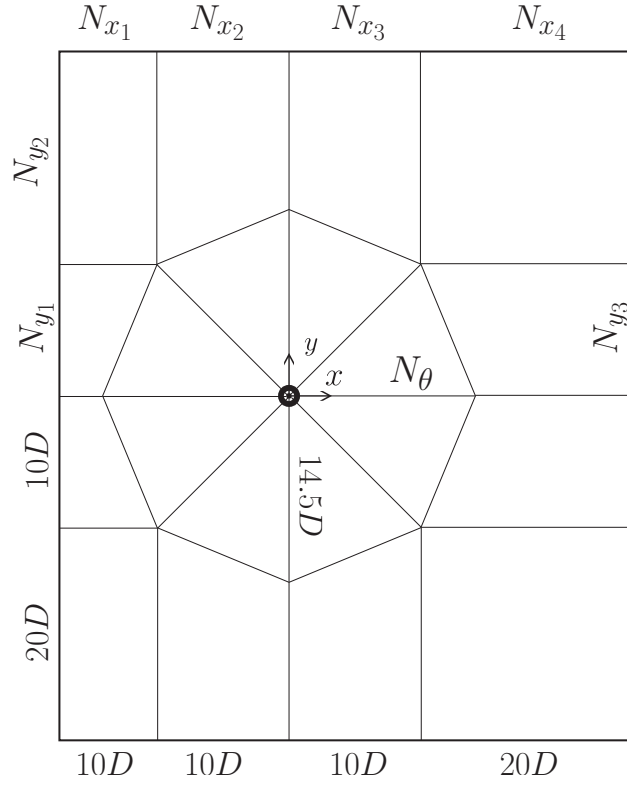


Figure 1: The computational domain for numerical simulations.  $N$  denotes the number of mesh points, where  $N_{x_1} = 20$ ,  $N_{x_2} = 30$ ,  $N_{x_3} = 50$ ,  $N_{x_4} = 50$ ,  $N_{y_1} = 30$ ,  $N_{y_2} = 30$ ,  $N_{y_3} = 80$ , and  $N_\theta = 150$ . The domain size and number of mesh points in the spanwise direction are  $6D$  and  $96$ .

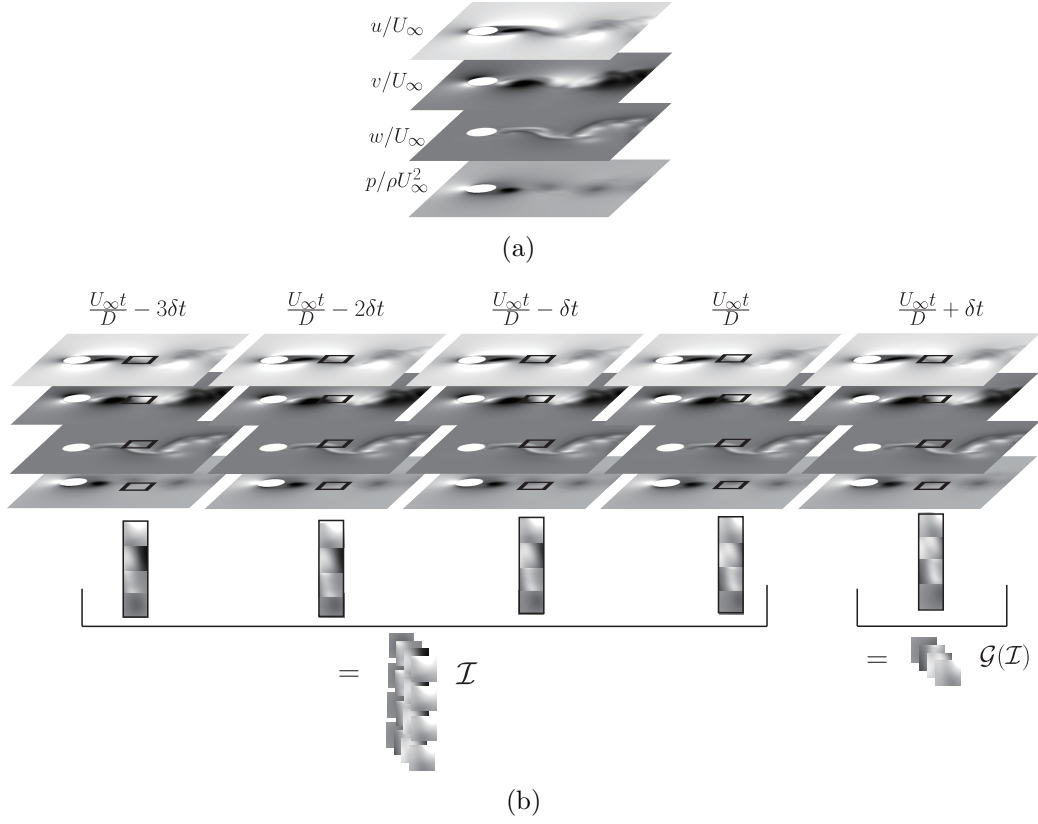


Figure 2: (a) Instantaneous flow variables of  $u/U_\infty, v/U_\infty, w/U_\infty, p/\rho U_\infty^2$  ( $250 \times 250$  sized grid and  $7D \times 7D$  sized domain). (b) The procedure of subsampling five consecutive flow fields to an input ( $\mathcal{I}$ ) and ground truth ( $\mathcal{G}(\mathcal{I})$ ) of a training sample on a  $32 \times 32$  sized grid and  $0.896 \times 0.896$  sized domain.

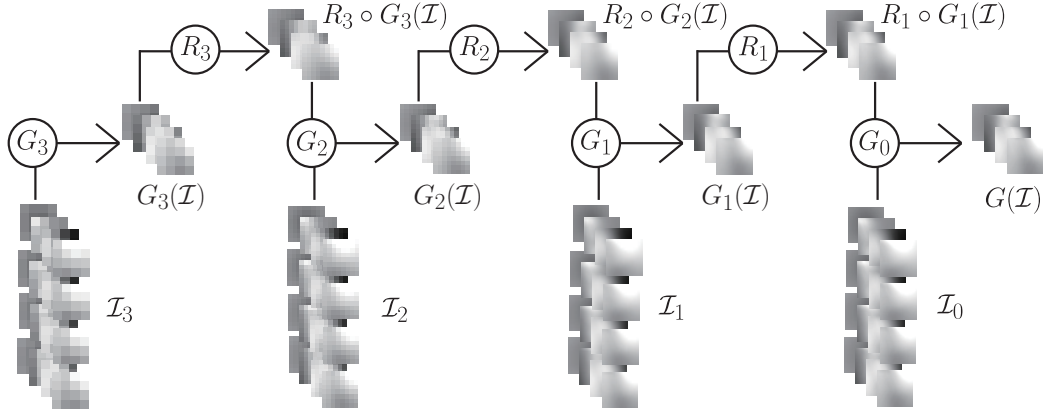


Figure 3: Schematic diagram of generator models.  $\mathcal{I}$  is the set of input flow fields and  $\mathcal{I}_k$  denotes interpolated input flow fields on a  $1/(2^k \times 2^k)$  smaller scale grid, while domain sizes are identical.  $G_k$  indicates a generative CNN which is fed with input  $I_k$ , while  $G_k(\mathcal{I})$  indicates the set of generated predictions of flow fields from generative CNN  $G_k$ .  $R_k$  indicates the rescale operator, which upscales the grid size twice in both height and width.

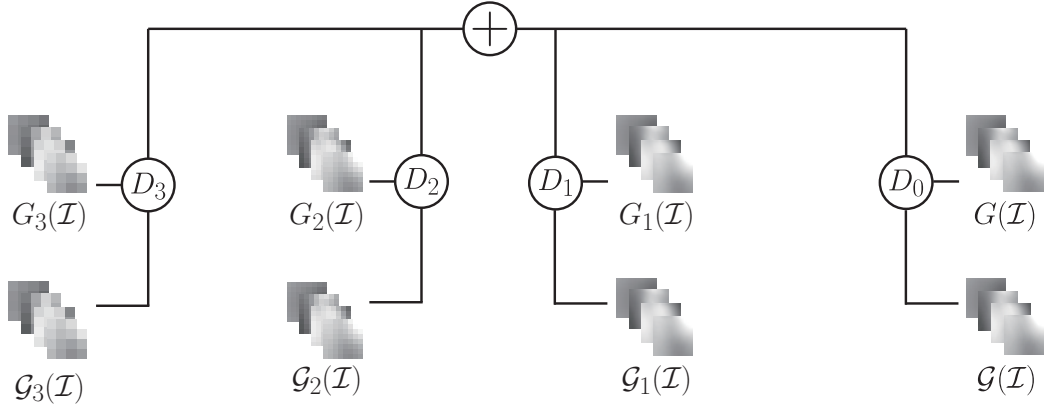


Figure 4: Schematic diagram of the discriminator model.  $D_k$  indicates the discriminative network which is fed with  $G_k(\mathcal{I})$  and  $\mathcal{G}_k(\mathcal{I})$ .  $G_k(\mathcal{I})$  indicates the set of generated predictions of flow fields from generative CNN  $G_k$ , while  $\mathcal{G}_k(\mathcal{I})$  indicates the set of ground truth flow fields.

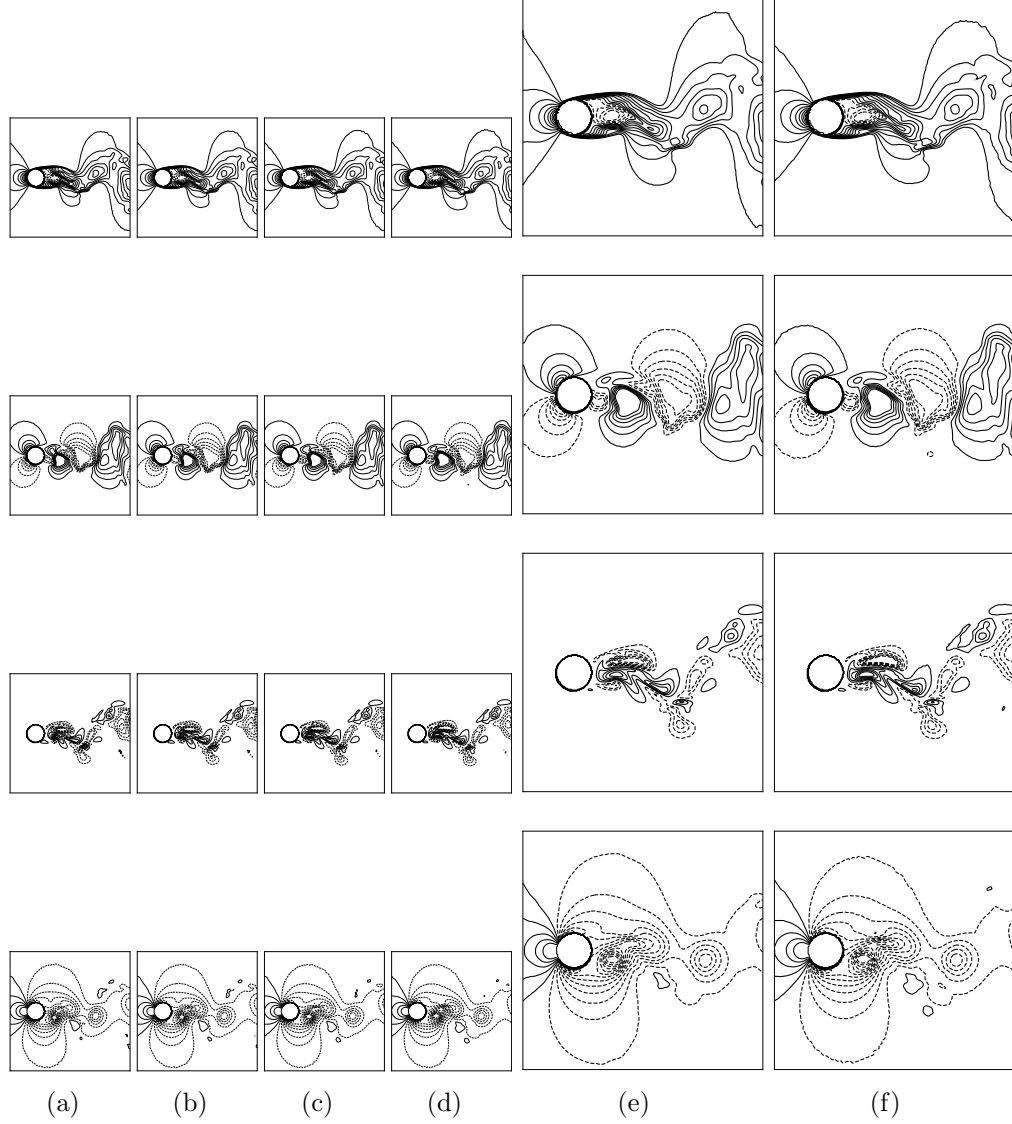


Figure 5: Comparison between the predicted and ground truth flow fields at test data ( $Re_D = 500$ ) using a generator model ( $GM_{20}$  and  $N_{64}$ ) based on supervised feature extraction without prior knowledge of physical conservation laws: (a-d) are the input sets of flow fields, where (e) and (f) are the predicted and ground truth flow fields. Each group of two rows from top to bottom indicate  $u/U_\infty$ ,  $v/U_\infty$ ,  $w/U_\infty$ , and  $p/\rho U_\infty^2$ . 15 contours for  $u/U_\infty$ ,  $v/U_\infty$ , and  $w/U_\infty$  are ranged from -0.5 to 1.0, -0.7 to 0.7, and -0.5 to 0.5. 20 contours for  $p/\rho U_\infty^2$  are ranged from -1.0 to 0.4. Solid line — and dotted line -- indicate positive and negative levels, respectively. The time-step interval between flow fields is  $\delta t = 0.01$ .

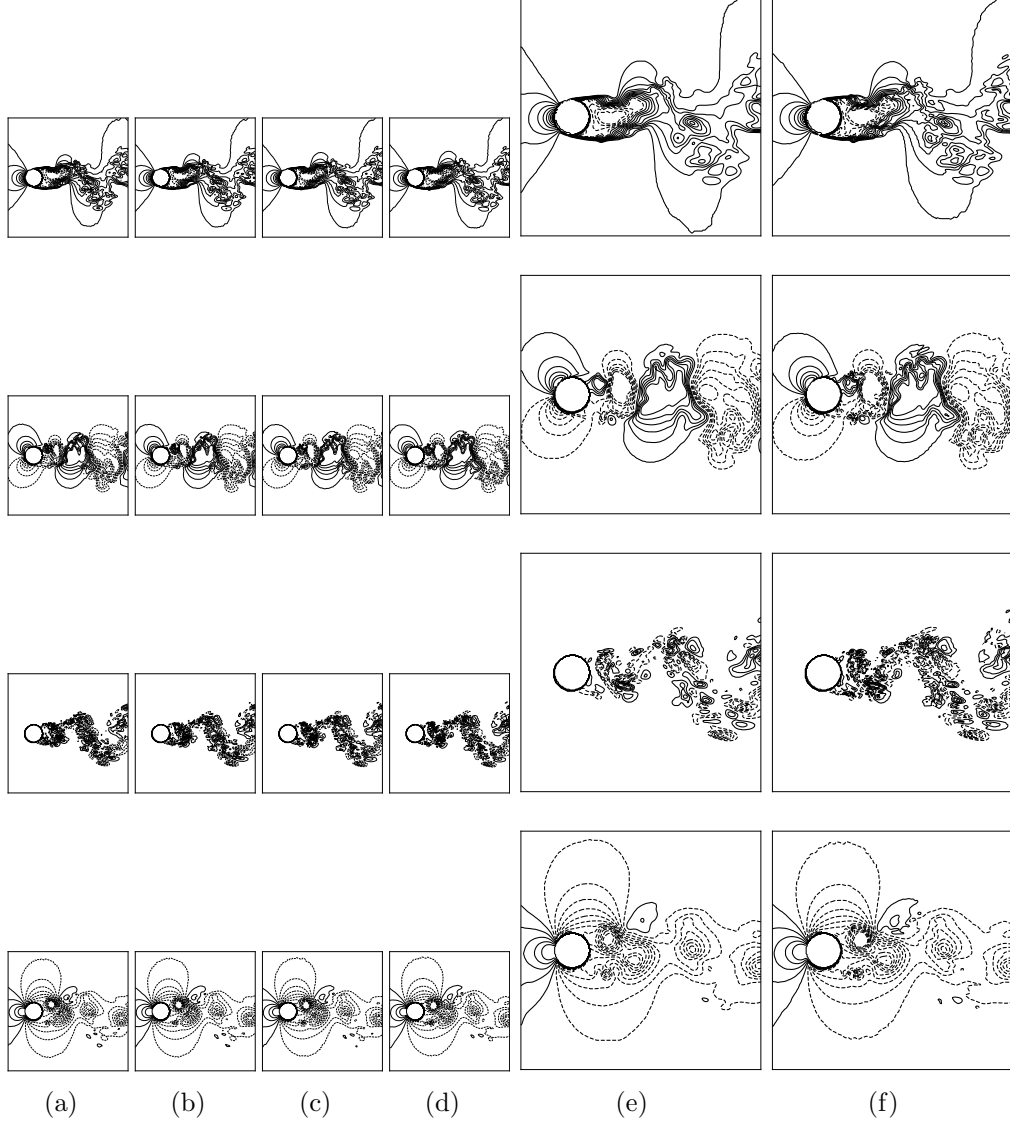


Figure 6: Comparison between the predicted and ground truth flow fields at test data ( $Re_D = 3000$ ) using a generator model ( $GM_{20}$  and  $N_{64}$ ) based on supervised feature extraction without prior knowledge of physical conservation laws: (a-d) are the input sets of flow fields, where (e) and (f) are the predicted and ground truth flow fields. Each group of two rows from top to bottom indicate  $u/U_\infty$ ,  $v/U_\infty$ ,  $w/U_\infty$ , and  $p/\rho U_\infty^2$ . 15 contours for  $u/U_\infty$ ,  $v/U_\infty$ , and  $w/U_\infty$  are ranged from -0.5 to 1.0, -0.7 to 0.7, and -0.5 to 0.5. 20 contours for  $p/\rho U_\infty^2$  are ranged from -1.0 to 0.4. Solid line — and dotted line -- indicate positive and negative levels, respectively. The time-step interval between flow fields is  $\delta t = 0.01$ .

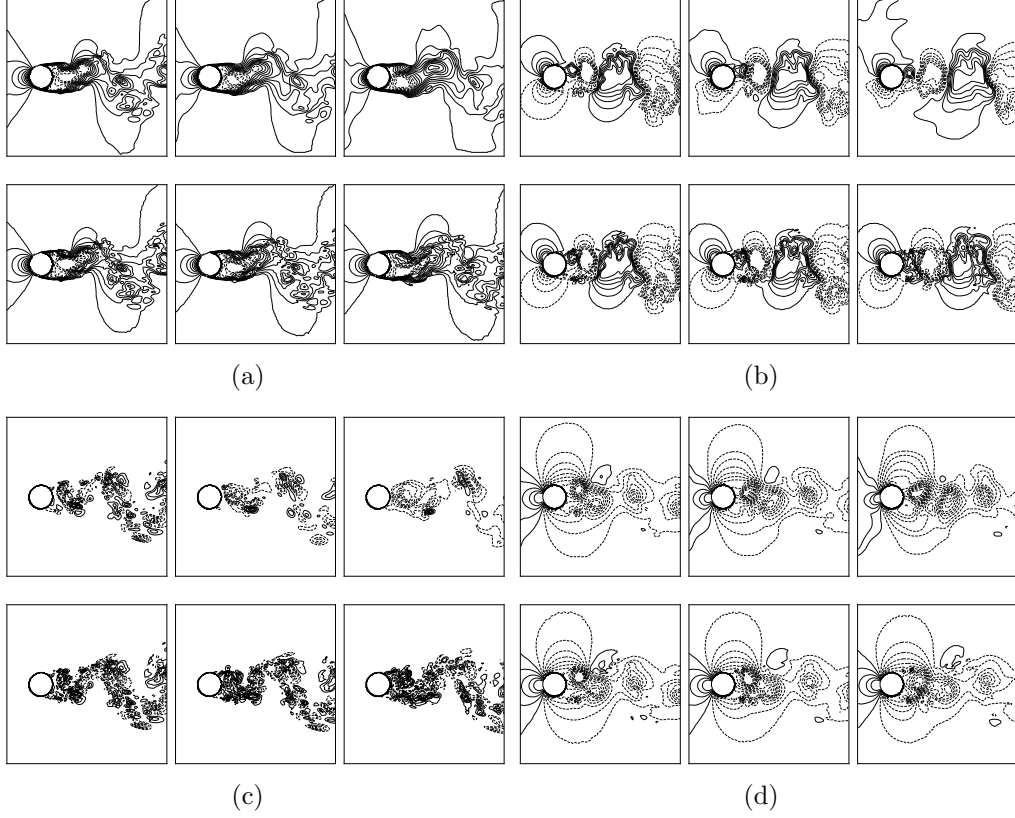


Figure 7: Comparison between the recursively predicted flow fields and ground truth flow fields of flow variables at  $Re_D = 3000$  using a generator model ( $GM_{20}$  and  $N_{64}$ ) based on supervised feature extraction without prior knowledge of physical conservation laws: (a)  $u/U_\infty$ , (b)  $v/U_\infty$ , (c)  $w/U_\infty$ , (d)  $p/\rho U_\infty^2$ . The first and second rows show the recursively predicted and ground truth flow fields after  $\delta t$ ,  $5\delta t$ ,  $10\delta t$  (from left to right). 15 contours for  $u/U_\infty$ ,  $v/U_\infty$ , and  $w/U_\infty$  are ranged from -0.5 to 1.0, -0.7 to 0.7, and -0.5 to 0.5. 20 contours for  $p/\rho U_\infty^2$  are ranged from -1.0 to 0.4. Solid line — and dotted line -- indicate positive and negative levels, respectively. The time-step interval between input flow fields is  $\delta t = 0.01$ .

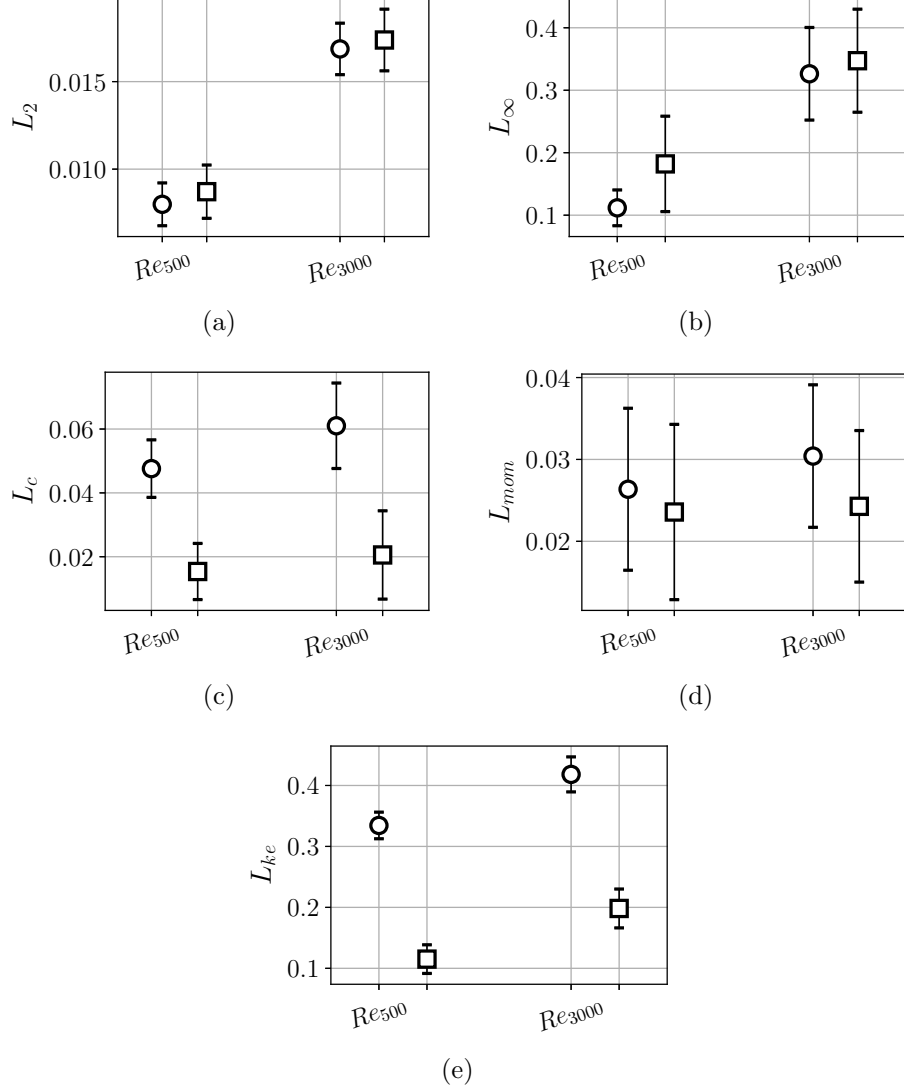


Figure 8: Comparison between errors from generator models with and without prior knowledge of physical conservation laws: (a) and (b) are the  $L_2$  and  $L_\infty$  errors; (c), (d), and (e) are the  $L_c$ ,  $L_{mom}$ , and  $L_{ke}$  errors.  $\circ$  denotes errors from a generator model based on supervised feature extraction without prior knowledge of physical conservation laws (configuration of  $GM_{20}$ , number set  $N_{64}$ ,  $\lambda_{l2} = \lambda_{gdl} = 0.5$  and  $\lambda_{adv} = \lambda_c = \lambda_{mom} = \lambda_{ke} = 0.0$ );  $\square$  denotes errors from a generator model based on supervised feature extraction with prior knowledge of physical conservation laws (configuration of  $GM_{20}$ , number set  $N_{64}$ ,  $\lambda_{l2} = \lambda_{gdl} = \lambda_c = \lambda_{mom} = \lambda_{ke} = 0.2$  and  $\lambda_{adv} = 0.0$ ). The errorbars represents the standard deviation.

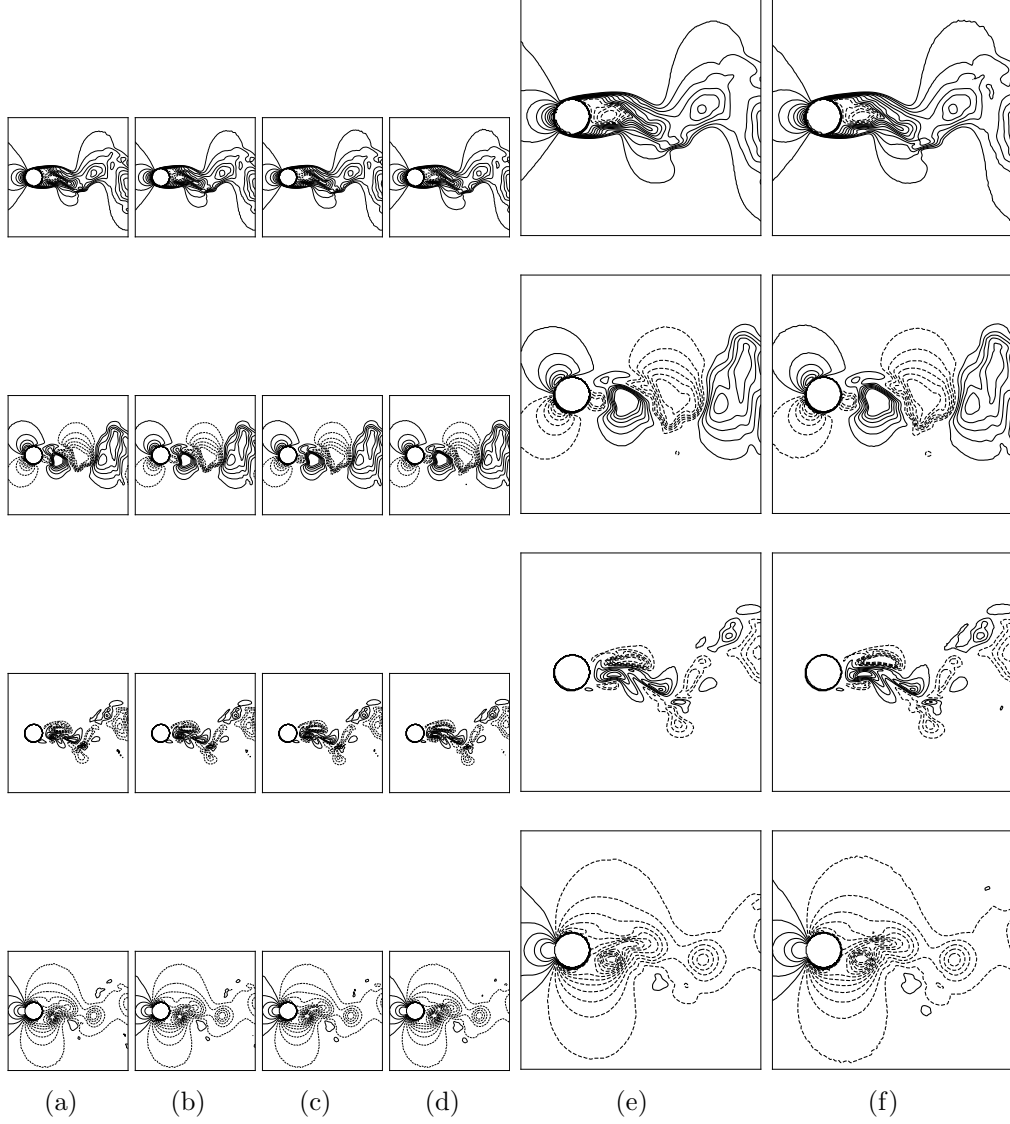


Figure 9: Comparison between the predicted and ground truth flow fields at test data ( $Re_D = 500$ ) using a generator model ( $GM_{20}$  and  $N_{64}$ ) with prior knowledge of physical conservation laws: (a-d) are the input sets of flow fields, where (e) and (f) are the predicted and ground truth flow fields. 15 contours for  $u/U_\infty$ ,  $v/U_\infty$ , and  $w/U_\infty$  are ranged from -0.5 to 1.0, -0.7 to 0.7, and -0.5 to 0.5. 20 contours for  $p/\rho U_\infty^2$  are ranged from -1.0 to 0.4. Solid line — and dotted line -- indicate positive and negative levels, respectively. The time-step interval between flow fields is  $\delta t = 0.01$ .

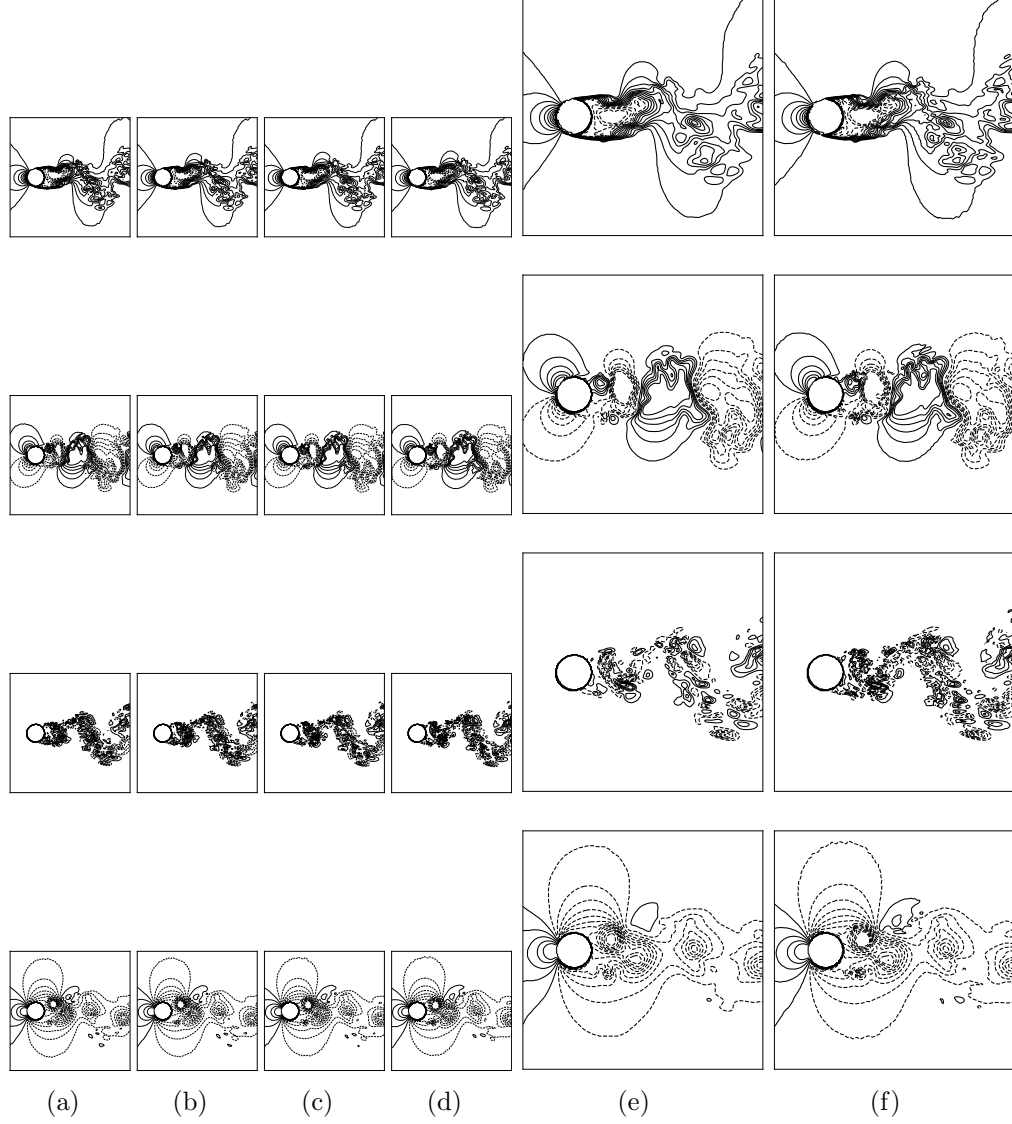


Figure 10: Comparison between the predicted and ground truth flow fields at test data ( $Re_D = 3000$ ) using a generator model ( $GM_{20}$  and  $N_{64}$ ) with prior knowledge of physical conservation laws: (a-d) are the input sets of flow fields, where (e) and (f) are the predicted and ground truth flow fields. 15 contours for  $u/U_\infty$ ,  $v/U_\infty$ , and  $w/U_\infty$  are ranged from -0.5 to 1.0, -0.7 to 0.7, and -0.5 to 0.5. 20 contours for  $p/\rho U_\infty^2$  are ranged from -1.0 to 0.4. Solid line — and dotted line -- indicate positive and negative levels, respectively. The time-step interval between flow fields is  $\delta t = 0.01$ .

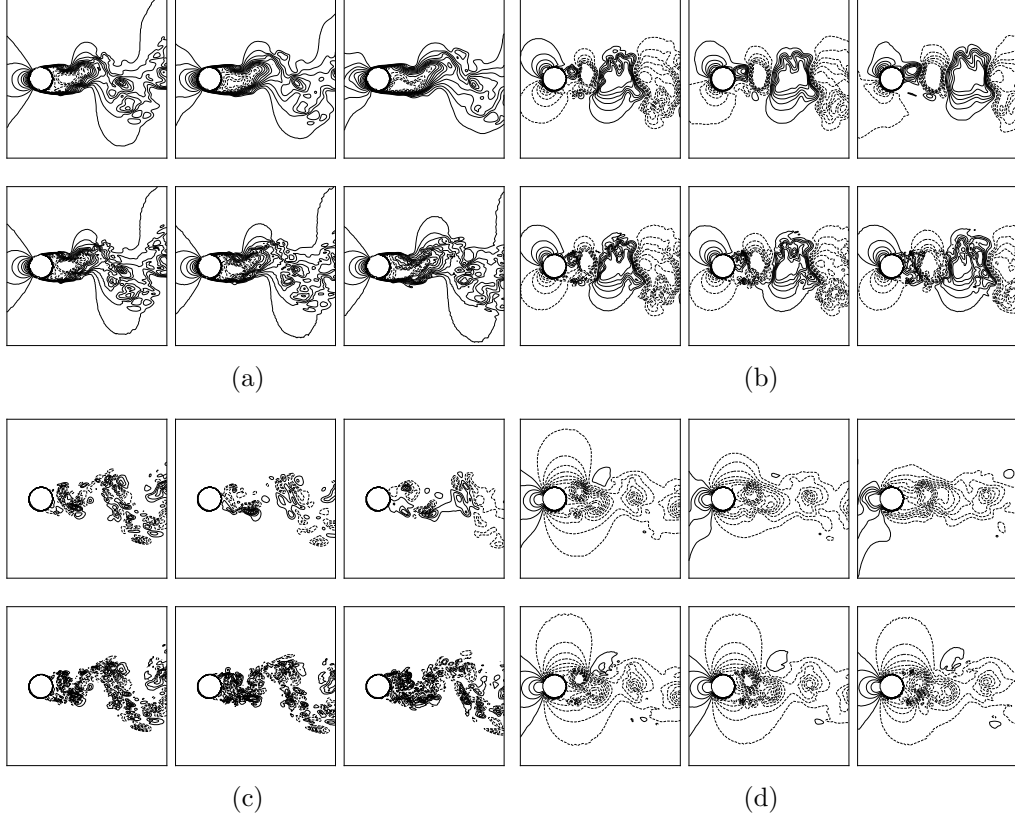
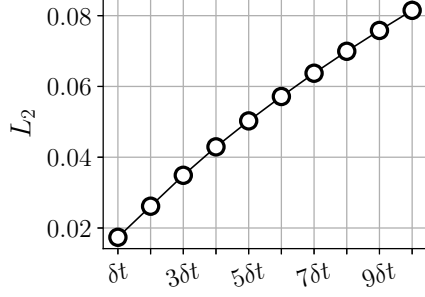
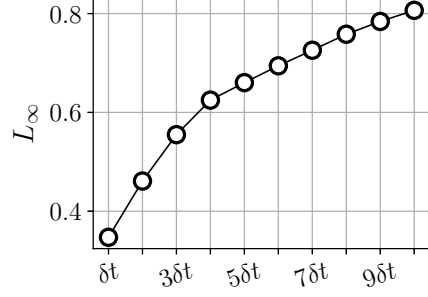


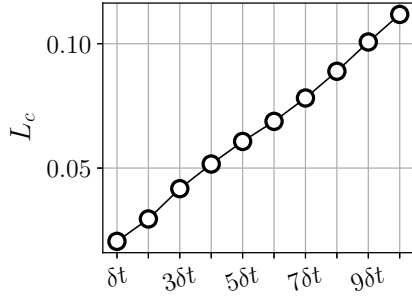
Figure 11: Comparison between the recursively predicted flow fields and ground truth flow fields of flow variables at  $Re_D = 3000$  using a generator model ( $GM_{20}$  and  $N_{64}$ ) with prior knowledge of physical conservation laws: (a)  $u/U_\infty$ , (b)  $v/U_\infty$ , (c)  $w/U_\infty$ , (d)  $p/\rho U_\infty^2$ . The first and second rows show the recursively predicted and ground truth flow fields after  $\delta t$ ,  $5\delta t$ ,  $10\delta t$  (from left to right). 15 contours for  $u/U_\infty$ ,  $v/U_\infty$ , and  $w/U_\infty$  are ranged from -0.5 to 1.0, -0.7 to 0.7, and -0.5 to 0.5. 20 contours for  $p/\rho U_\infty^2$  are ranged from -1.0 to 0.4. Solid line — and dotted line -- indicate positive and negative levels, respectively. The time-step interval between input flow fields is  $\delta t = 0.01$ .



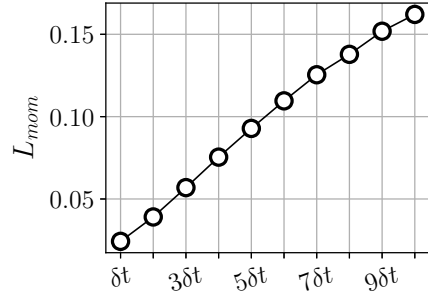
(a)



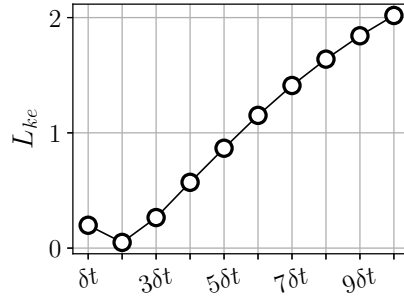
(b)



(c)

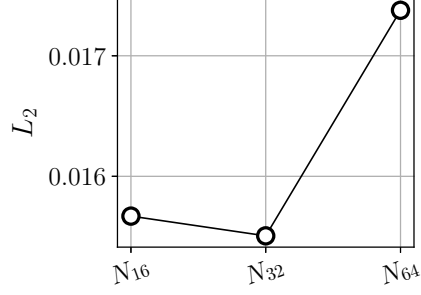


(d)

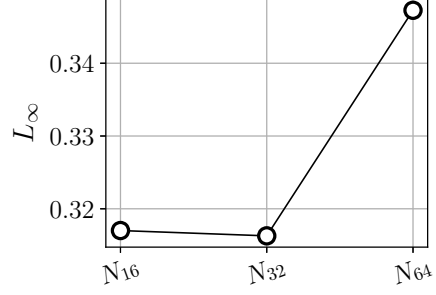


(e)

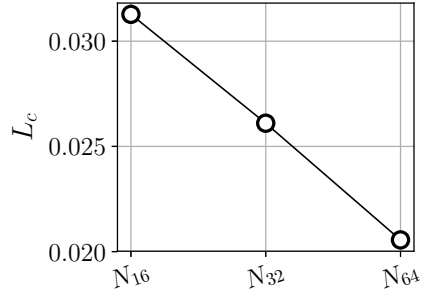
Figure 12: Flow prediction errors at  $Re_D = 3000$  respect to recursive prediction step using a generator model ( $GM_{20}$  and  $N_{64}$ ) with prior knowledge of physical conservation laws: (a) and (b) are the  $L_2$  and  $L_\infty$  errors; (c), (d), and (e) are the  $L_c$ ,  $L_{mom}$ , and  $L_{ke}$  errors.



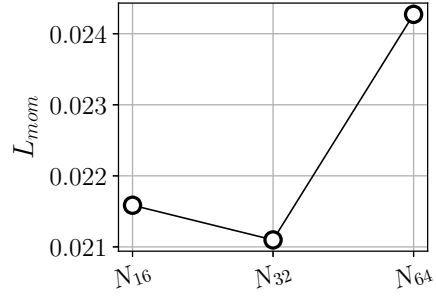
(a)



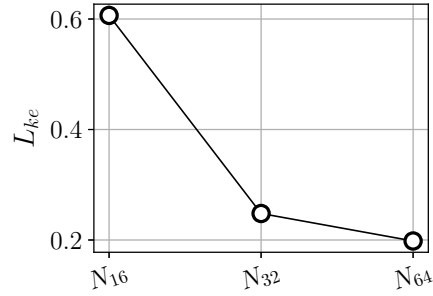
(b)



(c)

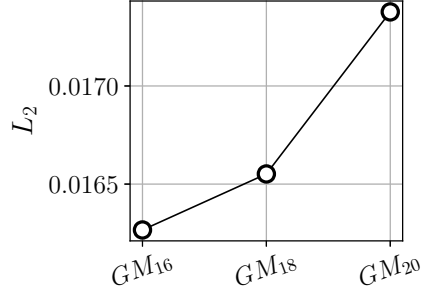


(d)

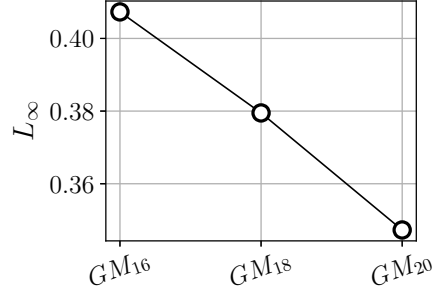


(e)

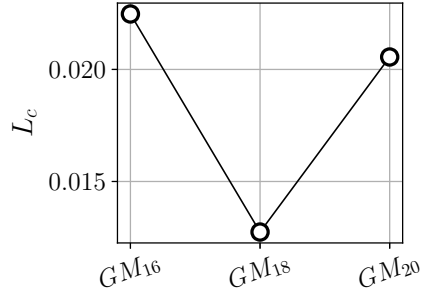
Figure 13: Flow prediction errors at  $Re_D = 3000$  respect to three cases of number set using generator models with prior knowledge of physical conservation laws: (a) and (b) are the  $L_2$  and  $L_\infty$  errors; (c), (d), and (e) are the  $L_c$ ,  $L_{mom}$ , and  $L_{ke}$  errors.



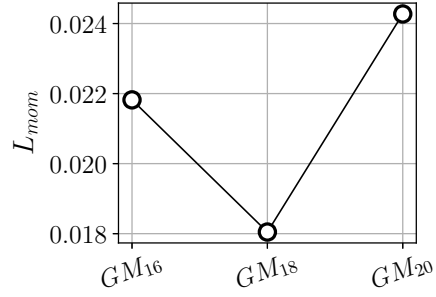
(a)



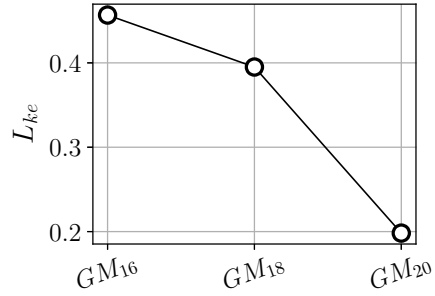
(b)



(c)

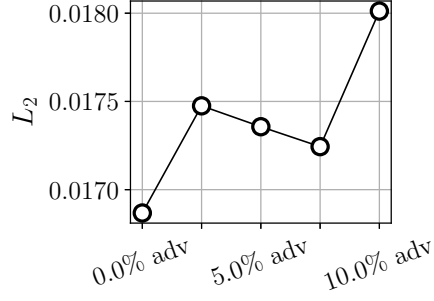


(d)

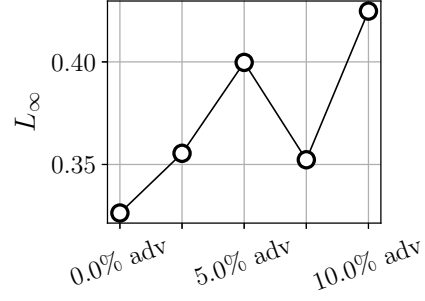


(e)

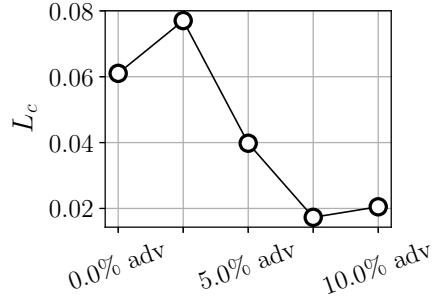
Figure 14: Flow prediction errors at  $Re_D = 3000$  respect to three cases of generator configuration with prior knowledge of physical conservation laws: (a) and (b) are the  $L_2$  and  $L_\infty$  errors; (c), (d), and (e) are the  $L_c$ ,  $L_{mom}$ , and  $L_{ke}$  errors.



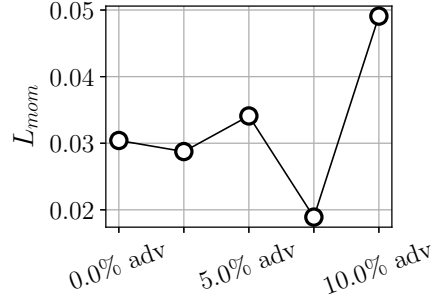
(a)



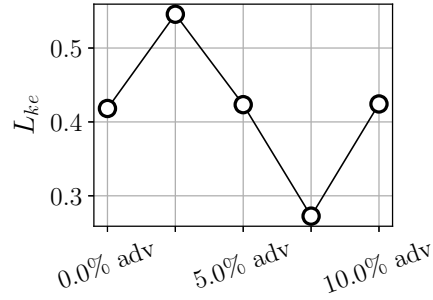
(b)



(c)



(d)



(e)

Figure 15: Flow prediction errors at  $Re_D = 3000$  respect to adversarial training percentage using a generator model ( $GM_{20}$  and  $N_{64}$ ): (a) and (b) are the  $L_2$  and  $L_\infty$  errors; (c), (d), and (e) are the  $L_c$ ,  $L_{mom}$ , and  $L_{ke}$  errors.

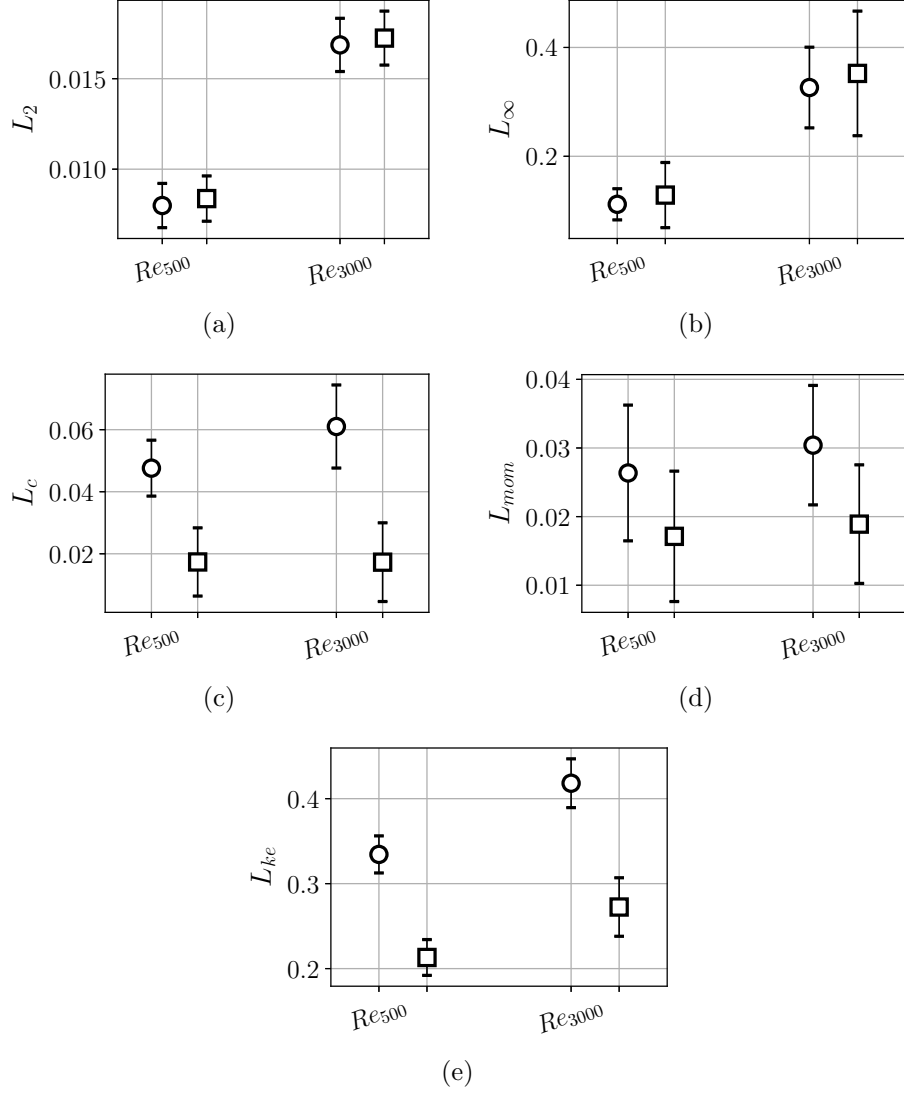


Figure 16: Comparison between errors from generator models with and without unsupervised feature extraction: (a) and (b) are the  $L_2$  and  $L_\infty$  errors; (c), (d), and (e) are the  $L_c$ ,  $L_{mom}$ , and  $L_{ke}$  errors.  $\circ$  denotes errors from a generator model based on supervised feature extraction without prior knowledge of physical conservation laws (configuration of  $GM_{20}$ , number set  $N_{64}$ ,  $\lambda_{l2} = \lambda_{gdl} = 0.5$  and  $\lambda_{adv} = \lambda_c = \lambda_{mom} = \lambda_{ke} = 0.0$ );  $\square$  denotes errors from a generator model associated with unsupervised feature extraction (configuration of  $GM_{20}$ , number set  $N_{64}$ ,  $\lambda_{l2} = \lambda_{gdl} = 0.4625$ ,  $\lambda_{adv} = 0.075$ , and  $\lambda_c = \lambda_{mom} = \lambda_{ke} = 0.0$ ). The errorbars represents the standard deviation.

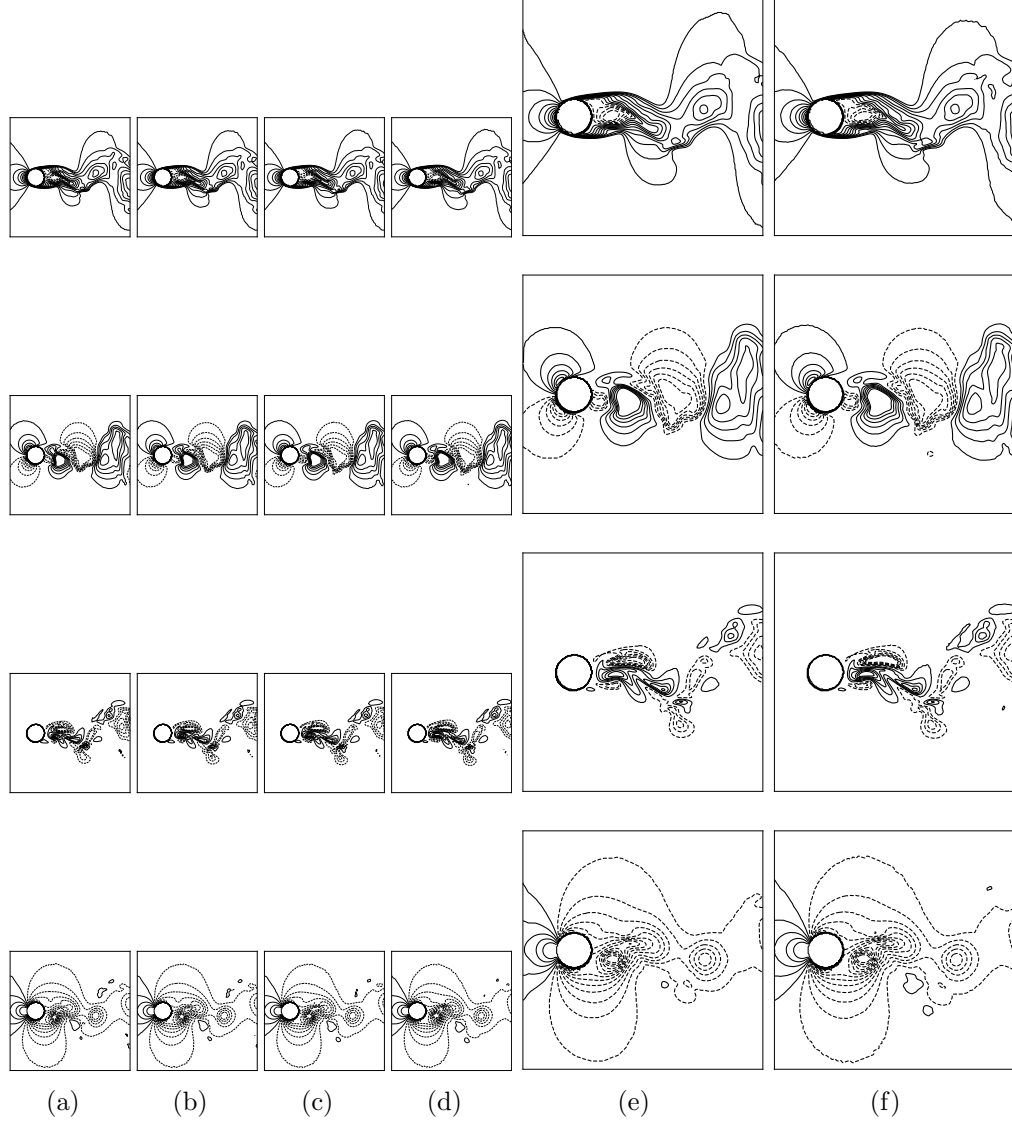


Figure 17: Comparison between the predicted and ground truth flow fields at test data ( $Re_D = 500$ ) using a generator model ( $GM_{20}$  and  $N_{64}$ ) associated with unsupervised feature extraction: (a-d) are the input sets of flow fields, where (e) and (f) are the predicted and ground truth flow fields. 15 contours for  $u/U_\infty$ ,  $v/U_\infty$ , and  $w/U_\infty$  are ranged from -0.5 to 1.0, -0.7 to 0.7, and -0.5 to 0.5. 20 contours for  $p/\rho U_\infty^2$  are ranged from -1.0 to 0.4. Solid line — and dotted line -- indicate positive and negative levels, respectively. The time-step interval between flow fields is  $\delta t = 0.01$ .

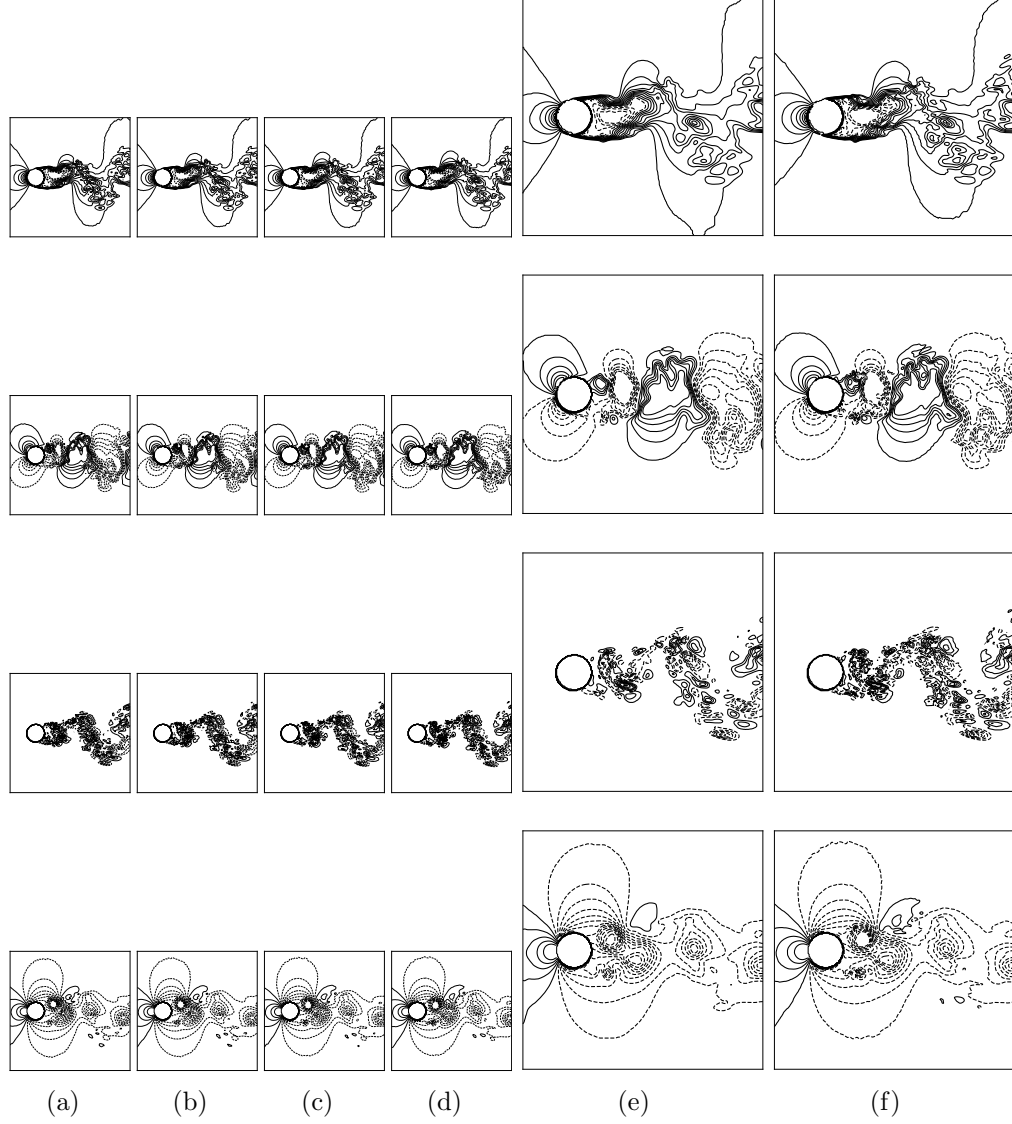


Figure 18: Comparison between the predicted and ground truth flow fields at test data ( $Re_D = 3000$ ) using a generator model ( $GM_{20}$  and  $N_{64}$ ) associated with unsupervised feature extraction: (a-d) are the input sets of flow fields, where (e) and (f) are the predicted and ground truth flow fields. 15 contours for  $u/U_\infty$ ,  $v/U_\infty$ , and  $w/U_\infty$  are ranged from -0.5 to 1.0, -0.7 to 0.7, and -0.5 to 0.5. 20 contours for  $p/\rho U_\infty^2$  are ranged from -1.0 to 0.4. Solid line — and dotted line -- indicate positive and negative levels, respectively. The time-step interval between flow fields is  $\delta t = 0.01$ .

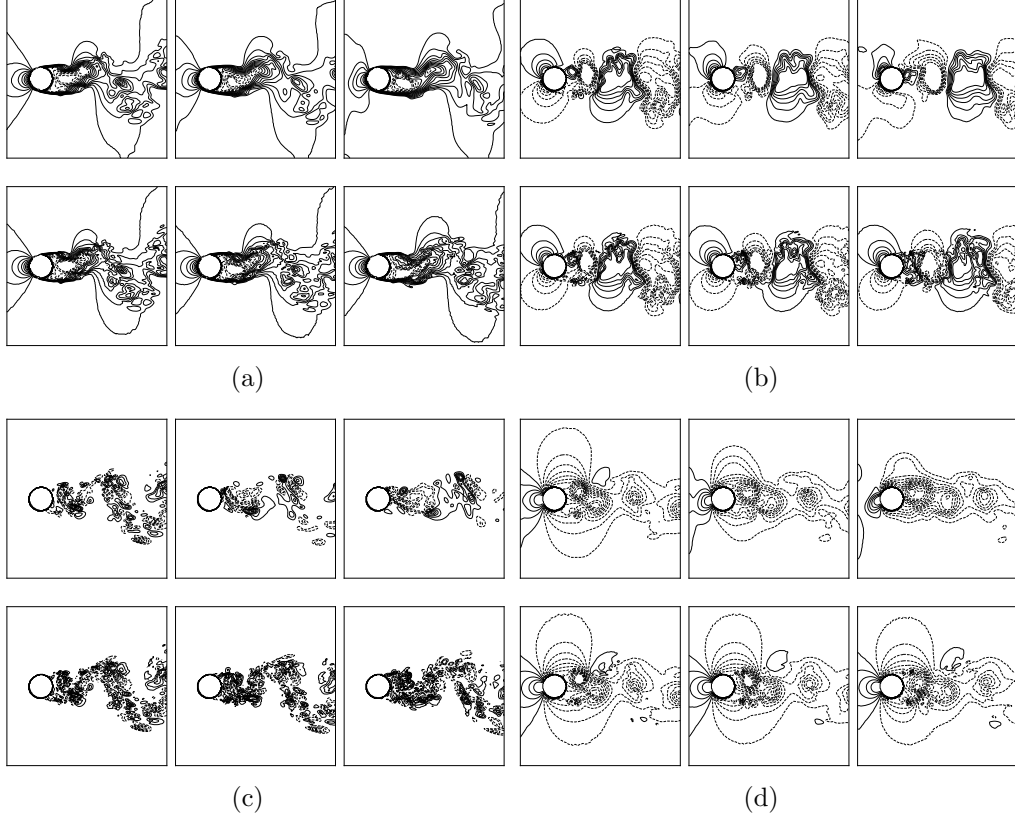
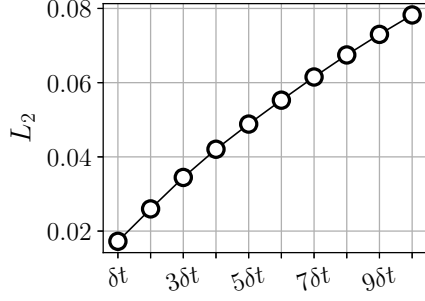
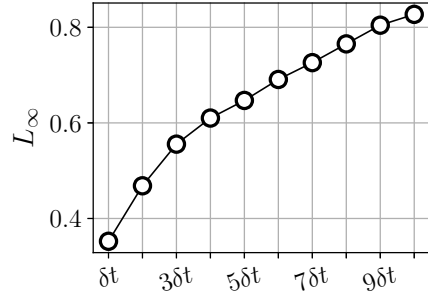


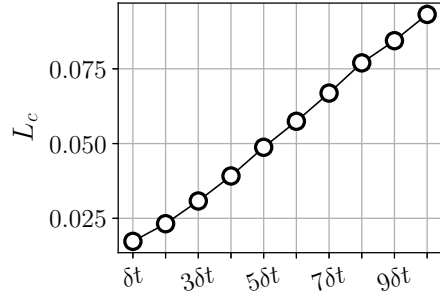
Figure 19: Comparison between the recursively predicted flow fields and ground truth flow fields of flow variables at  $Re_D = 3000$  using a generator model ( $GM_{20}$  and  $N_{64}$ ) associated with unsupervised feature extraction: (a)  $u/U_\infty$ , (b)  $v/U_\infty$ , (c)  $w/U_\infty$ , (d)  $p/\rho U_\infty^2$ . The first and second rows show the recursively predicted and ground truth flow fields after  $\delta t$ ,  $5\delta t$ ,  $10\delta t$  (from left to right). 15 contours for  $u/U_\infty$ ,  $v/U_\infty$ , and  $w/U_\infty$  are ranged from -0.5 to 1.0, -0.7 to 0.7, and -0.5 to 0.5. 20 contours for  $p/\rho U_\infty^2$  are ranged from -1.0 to 0.4. Solid line — and dotted line -- indicate positive and negative levels, respectively. The time-step interval between input flow fields is  $\delta t = 0.01$ .



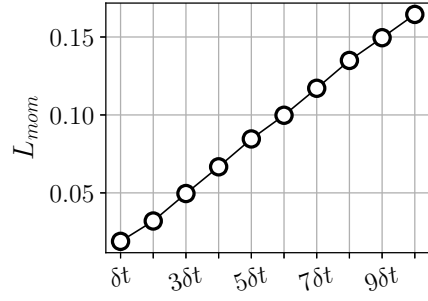
(a)



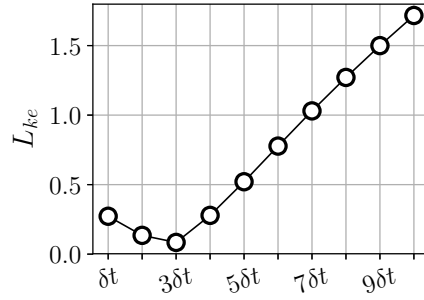
(b)



(c)

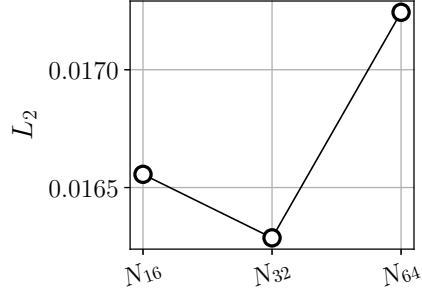


(d)

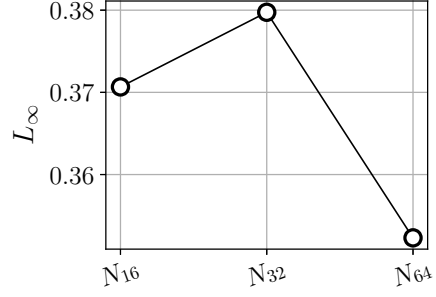


(e)

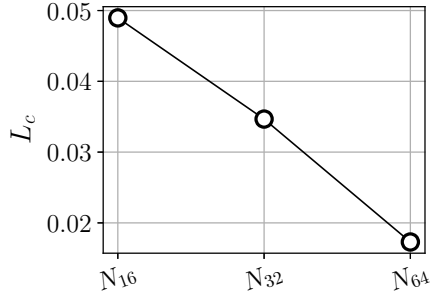
Figure 20: Flow prediction errors at  $Re_D = 3000$  respect to recursive prediction step using a generator model ( $GM_{20}$  and  $N_{64}$ ) associated with unsupervised feature extraction: (a) and (b) are the  $L_2$  and  $L_\infty$  errors; (c), (d), and (e) are the  $L_c$ ,  $L_{mom}$ , and  $L_{ke}$  errors.



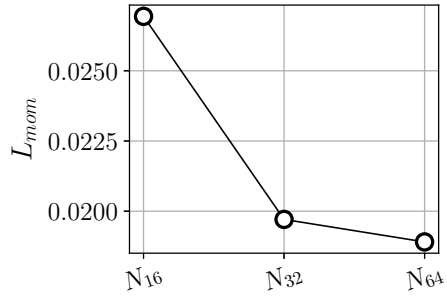
(a)



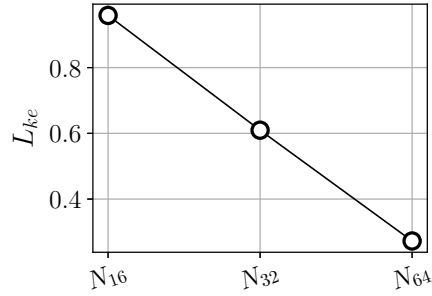
(b)



(c)

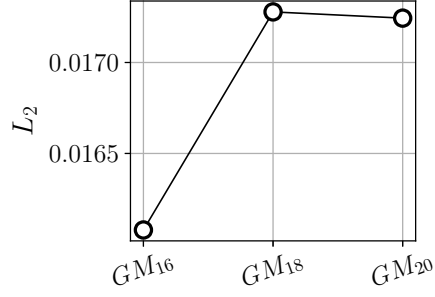


(d)

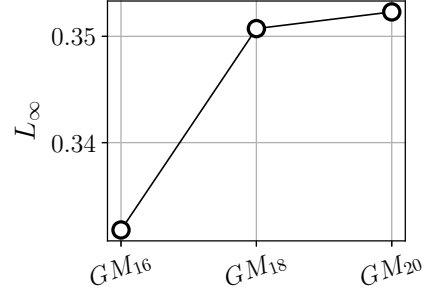


(e)

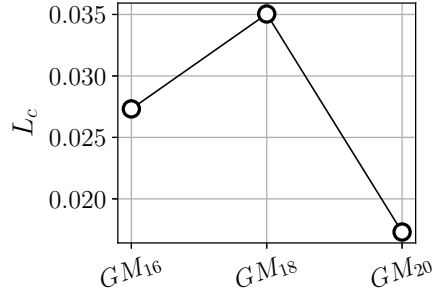
Figure 21: Flow prediction errors at  $Re_D = 3000$  respect to three cases of number set using generator models associated with unsupervised feature extraction: (a) and (b) are the  $L_2$  and  $L_\infty$  errors; (c), (d), and (e) are the  $L_c$ ,  $L_{mom}$ , and  $L_{ke}$  errors.



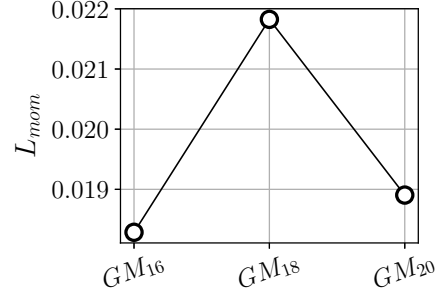
(a)



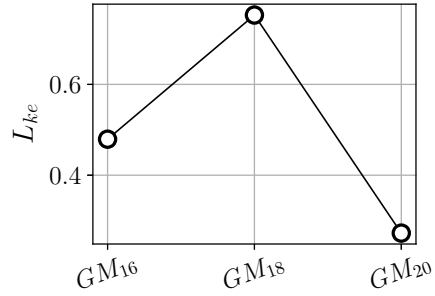
(b)



(c)



(d)



(e)

Figure 22: Flow prediction errors at  $Re_D = 3000$  respect to three cases of generator configuration associated with unsupervised feature extraction: (a) and (b) are the  $L_2$  and  $L_\infty$  errors; (c), (d), and (e) are the  $L_c$ ,  $L_{mom}$ , and  $L_{ke}$  errors.

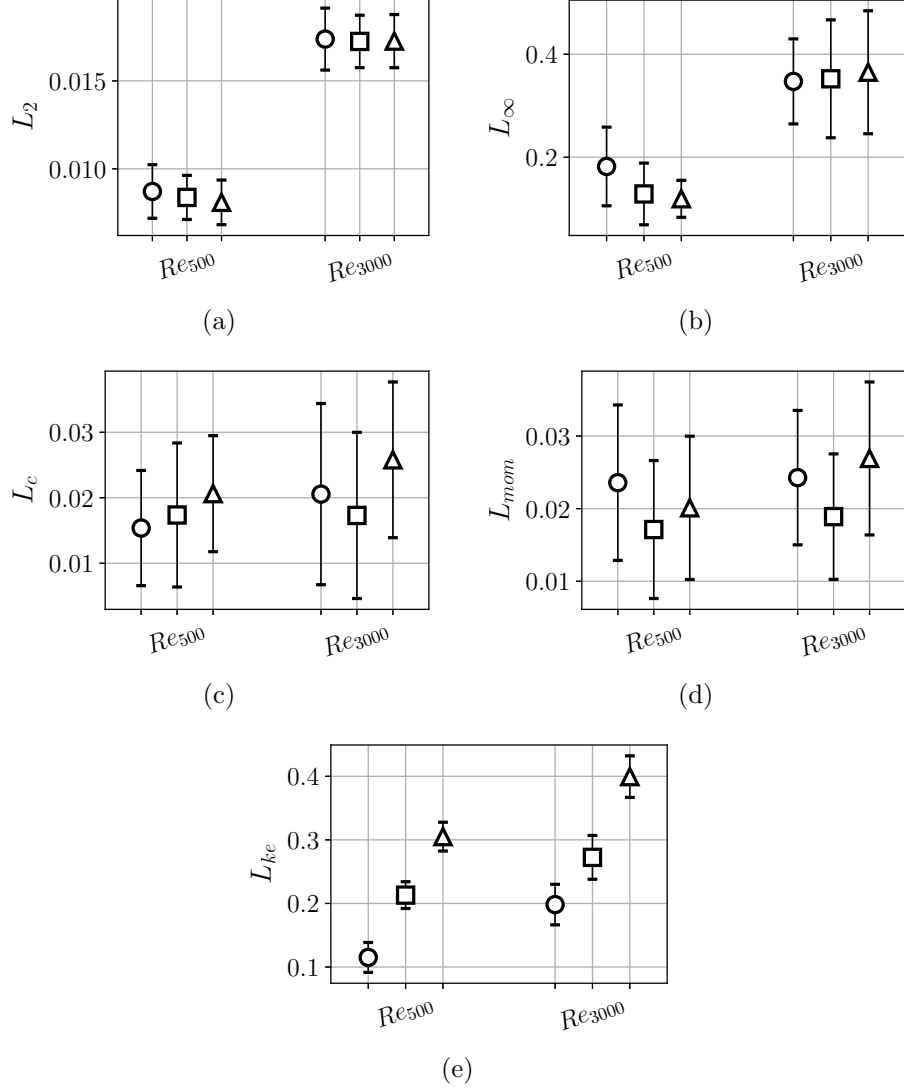


Figure 23: Comparison between errors from networks associated with unsupervised feature extraction with and without prior knowledge of physical conservation laws: (a) and (b) are the  $L_2$  and  $L_\infty$  errors; (c), (d), and (e) are the  $L_c$ ,  $L_{mom}$ , and  $L_{ke}$  errors. ○ denotes errors from a generator model with prior knowledge of physical conservation laws (configuration of  $GM_{20}$ , number set  $N_{64}$ ,  $\lambda_{l2} = \lambda_{gdl} = \lambda_c = \lambda_{mom} = \lambda_{ke} = 0.2$  and  $\lambda_{adv} = 0.0$ ); □ denotes errors from a generator model associated with unsupervised feature extraction (configuration of  $GM_{20}$ , number set  $N_{64}$ ,  $\lambda_{l2} = \lambda_{gdl} = 0.4625$ ,  $\lambda_{adv} = 0.075$ , and  $\lambda_c = \lambda_{mom} = \lambda_{ke} = 0.0$ ); △ denotes errors from a generator model with both unsupervised feature extraction and prior knowledge of physical conservation laws (configuration of  $GM_{20}$ , number set  $N_{64}$ ,  $\lambda_{l2} = \lambda_{gdl} = \lambda_c = \lambda_{mom} = \lambda_{ke} = 0.185$  and  $\lambda_{adv} = 0.075$ ). The errorbars represents the standard deviation.

## Highlights

Unsteady flow fields over a circular cylinder are trained and predicted using four deep learning networks: networks associated with supervised feature extraction with and without prior knowledge of physical conservation laws, networks associated with unsupervised feature extraction with and without prior knowledge of conservation laws. Flow fields at Reynolds numbers 100, 200, 300, and 400 are trained, while flow fields at Reynolds numbers 500 and 3000 are predicted. Physical loss functions are proposed and applied to explicitly provide prior knowledge of physical conservation laws to deep learning networks, while adversarial training is applied to extract features of physical conservation laws on data in an unsupervised manner. Predictions of unsteady flow fields using deep learning networks show good agreements with flow fields calculated by numerical simulations. Especially, results from adversarial training shows that physical conservation laws are successfully learned even without prior knowledge of physics. Thus, unsupervised learning based methods can be applied to learn undiscovered prior knowledge in data, where many practical data lacks information of the full underlying physics. Similar learning procedure can be applied to various practical usages, such as flow field predictions for control and guidance of aero- or hydro-vehicles and weather forecast.